


## Article

# Origin, Migration, and Characterization of Gas in the Xinglongtai Area, Liaohe Subbasin (Northeast China): Insight from Geochemical Evidence and Basin Modeling

Sibo Yang <sup>1</sup> , Meijun Li <sup>1,2,\*</sup>, Yanshan Wang <sup>3</sup>, Hong Xiao <sup>1</sup>, Shuangquan Huang <sup>3</sup>, Wujiang Kang <sup>3</sup> and Fangzheng Wang <sup>4</sup>

<sup>1</sup> National Key Laboratory of Petroleum Resources and Engineering, College of Geosciences, China University of Petroleum, Beijing 102249, China; susan\_44@live.cn (S.Y.); hongxiao@cup.edu.cn (H.X.)

<sup>2</sup> College of Petroleum, China University of Petroleum-Beijing at Karamay, Karamay 834000, China

<sup>3</sup> Research Institute of Petroleum Exploration and Development, Liaohe Oilfield Company, PetroChina, Panjin 124010, China

<sup>4</sup> No. 3 Gas Production Plant, Changqing Oilfield Company, PetroChina, Ordos 017000, China

\* Correspondence: meijunli@cup.edu.cn

**Abstract:** Buried hill zones in the rift basins have a significant impact on the enrichment of natural gas resources, and this is of great significance for exploration and development. This study aims to unravel the origins, migration, and dynamic accumulation process of natural gas in the Xinglongtai structural belt, Liaohe Subbasin. A comprehensive geological and geochemical analysis was performed on source rocks and natural gas samples from various geological structures within the Xinglongtai structural belt. Moreover, basin modeling techniques were employed to trace the genesis and migration of natural gas, offering an in-depth understanding of the dynamic process of accumulation. We identified the Fourth Mbr (Es<sub>4</sub>) and Third Mbr (Es<sub>3</sub>) of the Shahejie Fm as the main source rocks in the Qingshui and Chenjia Sags. The Es<sub>4</sub>, primarily Shallow Lacustrine Mudstones, contributed mainly type II organic matter, while the Es<sub>3</sub>, consisting of Nearshore Subaqueous Fan and Deep Lacustrine Mudstones, contributed mainly type III and type II organic matter, respectively. Two distinct hydrocarbon accumulation systems were observed, one inside and one outside the buried hills. The system outside the buried hill is governed by a complex fault system within the lacustrine basin, resulting in dual-source directions, dual-source rock types, two migration phases, and late-stage accumulation. In contrast, the system within the buried hill primarily involves reservoirs nested in the basement, exhibiting dual-source directions, dual-source rock types, a single migration phase, and early-stage charging. The understanding of this interplay, alongside dynamic simulation of generation, migration, and accumulation, can provide valuable insights for predicting natural gas distribution and accumulation patterns in terrestrial faulted lacustrine basins. This knowledge can guide more effective exploration and development strategies for natural gas.

**Keywords:** Lacustrine-rift basins; gas-source correlation; natural gas genetic type; gas generation–migration–accumulation modeling; effective gas source rocks; mixed genetic gas; the Xinglongtai structural belt



**Citation:** Yang, S.; Li, M.; Wang, Y.; Xiao, H.; Huang, S.; Kang, W.; Wang, F. Origin, Migration, and Characterization of Gas in the Xinglongtai Area, Liaohe Subbasin (Northeast China): Insight from Geochemical Evidence and Basin Modeling. *Energies* **2023**, *16*, 6429. <https://doi.org/10.3390/en16186429>

Academic Editor: Hossein Hamidi

Received: 31 July 2023

Revised: 16 August 2023

Accepted: 1 September 2023

Published: 5 September 2023



**Copyright:** © 2023 by the authors. Licensee MDPI, Basel, Switzerland. This article is an open access article distributed under the terms and conditions of the Creative Commons Attribution (CC BY) license (<https://creativecommons.org/licenses/by/4.0/>).

## 1. Introduction

A buried hill refers to the geological structure where ancient topographical highs are buried under younger strata unconformably. In rift basins, intense fault activity can lead to differential subsidence of the basement, forming ancient, buried hill structures [1]. These buried hill zones in rift basins are often highly prolific in oil and gas due to the favorable conditions and spaces they provide for the accumulation of hydrocarbons [2,3].

The Xinglongtai buried hill large-scale oil and gas field in the central and southern parts of the Western Depression, Liaohe Subbasin, located in the Bohai Bay Basin, is a quintessential

onshore overburden-type buried hill oil field [4–7]. It is nestled among two critical sags, which facilitates an abundant supply of oil and gas to this area. Yet, while the predominant belief is that the substantial quantity of humic-type gas generated in the inner Xinglongtai buried hill originates from the Shahejie Formation (Fm) source rocks, it should be noted that these source rocks mainly consist of type II organic matter, which includes contributions from both sapropelic and mixed sapropelic–humic components [7–9]. This fact presents a contradiction since humic-type gas is typically associated with humic organic matter [10]. In addition, the hydrocarbon accumulation conditions of gas fields in the inner Xinglongtai buried hill are relatively stringent due to poor reservoir development and strict requirements for hydrocarbon charging and migration [3,4,11,12]. The accumulation of the natural gas reservoir of the Xinglongtai structural belt (inner and outer buried hill) has the characteristics of multiple sources (multiple directions), multi-period hydrocarbon supply, multi-channel conduction, multi-layer system accumulation, multi-genetic trapping, and multi-stage accumulation [6]. However, specific research on the coupling relationship between the various accumulation elements of the Xinglongtai structural belt natural gas field at different periods is lacking. As a result, this poses a challenge for explorers in reasonably estimating the remaining exploration potential.

This study aims to clarify the origins and evolutionary process of natural gas by identifying the changes in the types of organic matter found in the source rocks of the Xinglongtai structural belt hydrocarbon supply sags. Through studying the dynamic mechanisms of natural gas accumulation using geochemical evidence and basin modeling techniques, our objective is to gain a more comprehensive understanding of the accumulation process and evolutionary history of the gas field in the Xinglongtai structural belt. This research will contribute to an understanding of the potential of natural gas resources in this area, providing a scientific basis for future exploration and development of the gas field in the Xinglongtai structural belt. Additionally, it may serve as a reference for studies on other similar gas reservoirs with an inner and outer buried hill.

## 2. Geological Setting

The Liaohe Subbasin is situated in the northeastern part of the Bohai Bay Basin and is subdivided into three depressions: the Western, Eastern, and Damintun Depressions (Figure 1a,b). Specifically, the Xinglongtai area lies within the middle of the Western Depression (Figure 1b). It constitutes a structural belt extending in the northeast direction and is surrounded by the Qingshui, Chenjia, and Panshan Sags (Figure 1c). The basement rocks of the Xinglongtai area comprise Archean metamorphic and magmatic rocks as well as Mesozoic volcanic eruptive and sedimentary rocks. The Paleogene strata incorporate the Fangshenpao (Ef) and Shahejie (Es) Formations—the latter is further divided into fourth (Es<sub>4</sub>), third (Es<sub>3</sub>), and second-first (Es<sub>1+2</sub>) members—along with the Dongying (Ed) Formation. Conversely, the Neogene strata include the Guantao (Ng) and Minghu zhen (Nm) Formations (Figure 2).

The Western Depression of the Liaohe Subbasin has undergone several significant tectonic phases throughout its formation and evolution. The movements since the Neogene can be further classified into three primary stages: the Eocene rifting phase (58.0–33.9 Ma), the Oligocene transition phase (33.9–23.03 Ma), and the Miocene sag phase (23.0–0 Ma). Each of these stages led to the formation of distinct fault structures (Figure 2) [13].

During the Eocene rifting phase, the tectonic activity was predominantly characterized by normal faults that had a north-northeast to northeast strike. These faults were widely distributed across the depression, extending downwards into the basement and upwards towards the top or within the Es<sub>3</sub> Formation. In the Oligocene transition phase, tectonic activity was primarily typified by normal faults with a north-east-east strike and a near east-west direction. The faults from this phase extended downwards to the Es Formation and upwards to the Ed Formation and its top (Figure 3). Lastly, during the Neogene-Quaternary period, tectonic activity consisted of a mix of north-northeast to northeast faults (including normal faults, reverse faults, and reversed faults), as well as a large number of east-west

normal faults. This stage exhibited a shift in fault orientations and activities, indicating a change in the dominant tectonic movements [14,15].

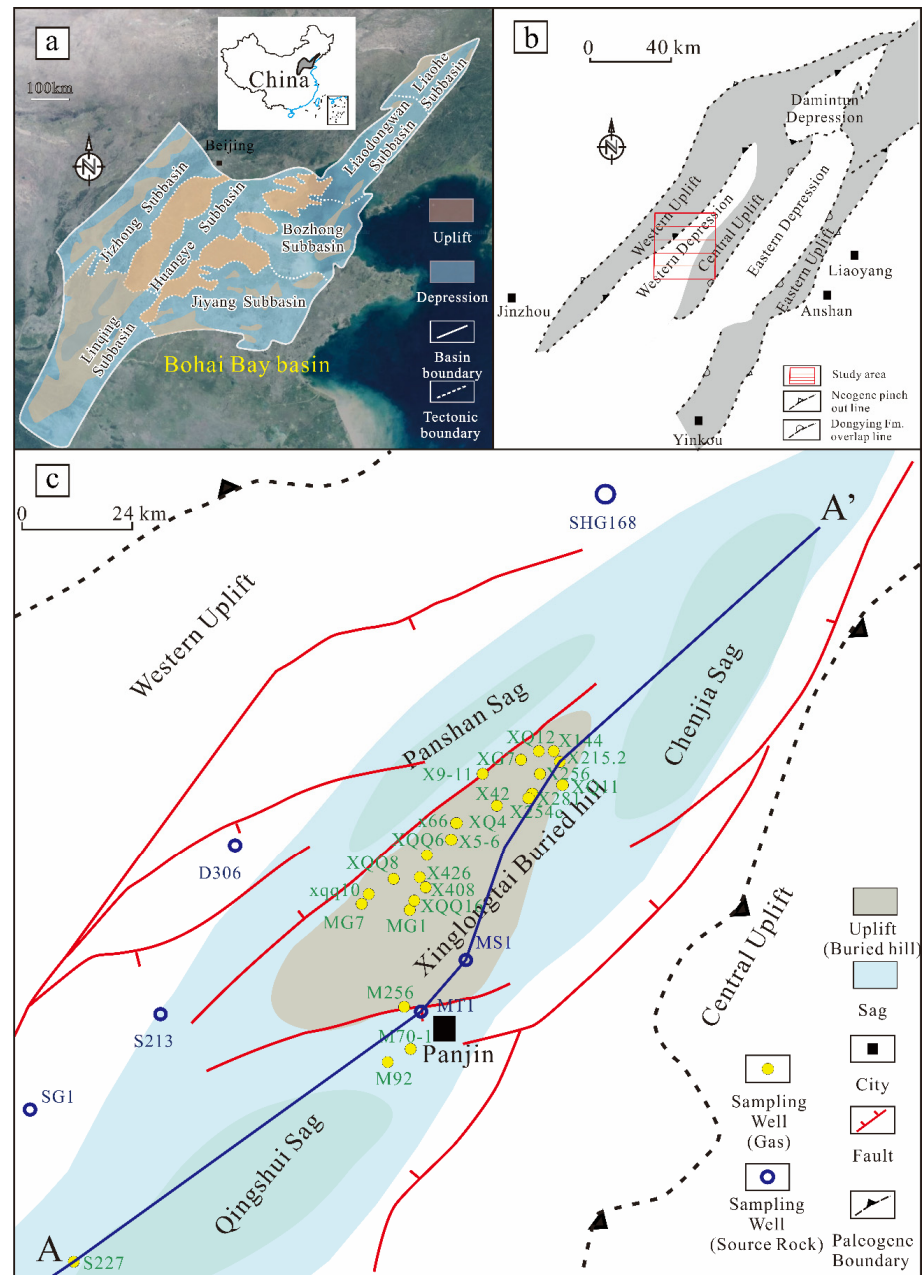


**Figure 1.** (a,b) show the location of the Xinglongtai area, Western Depression, Liaohe Subbasin. (c) Structural division of the Xinglongtai area.

The Western Depression predominantly features four types of sedimentary systems: Fan-delta, Sublacustrine-fan, Lacustrine, and Nearshore Subaqueous Fan sedimentation [9,16]. Within the Xinglongtai structural belt,  $E_3$  primarily consists of Nearshore Subaqueous Fan and Lacustrine sedimentation. The former refers to a sedimentary system composed of gravity flow sediments present in deep water-fan sedimentary systems. In contrast,  $E_4$  and  $E_2$  are mainly characterized by Fan-delta and Lacustrine facies sedimentation [17].

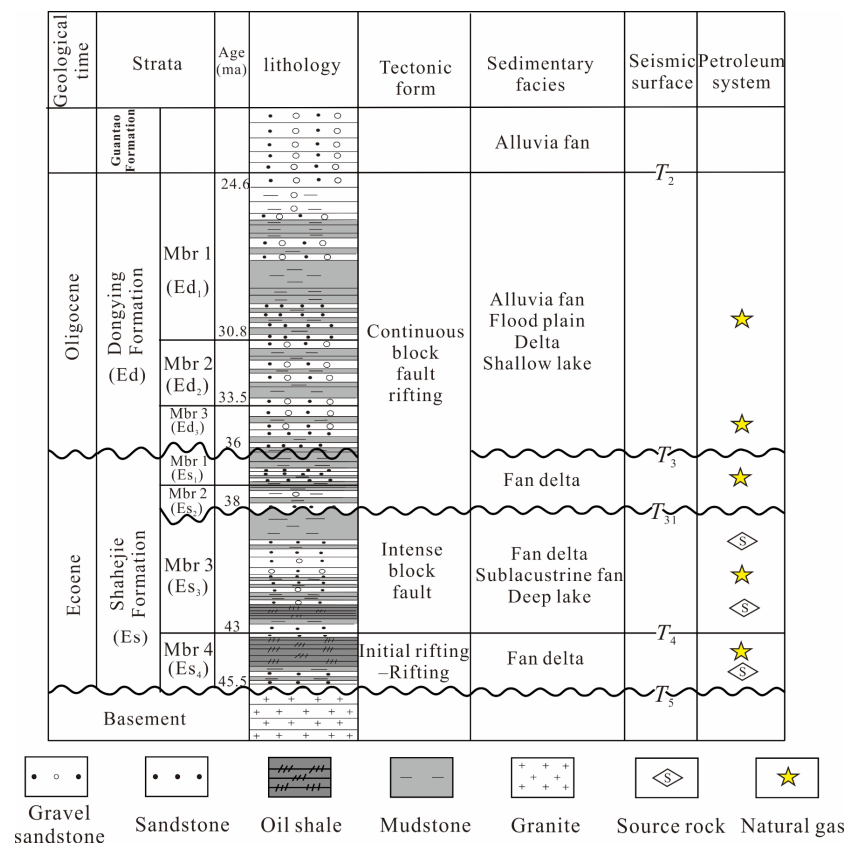


**Figure 2.** Generalized stratigraphy of the Western Depression, Bohai Bay Basin, modified after [14]. Source rocks and major gas reservoirs are marked.

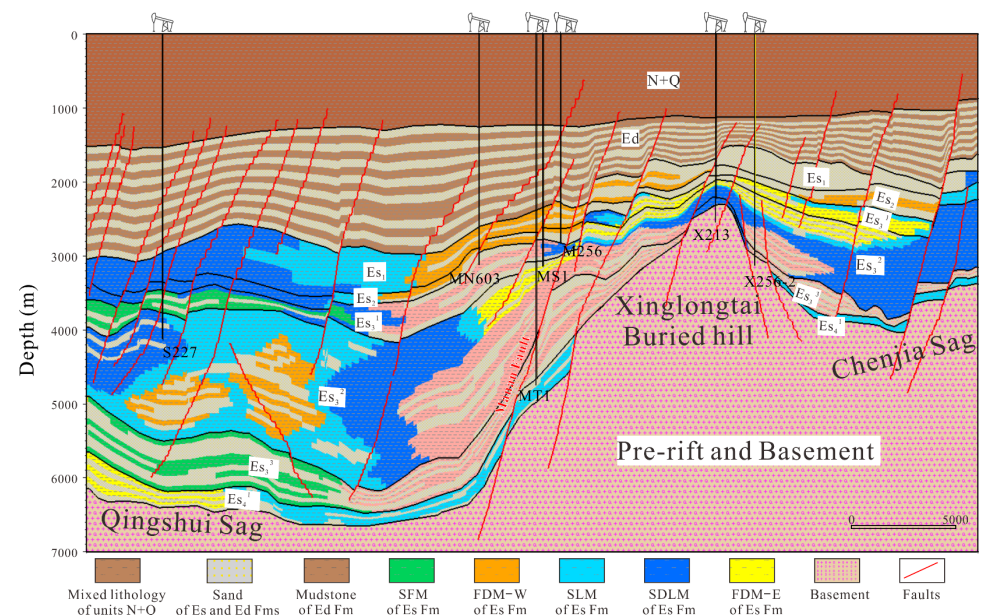


**Figure 3.** Two-dimensional lithofacies models for three representative profiles. The locations are illustrated in Figure 1b. SFM = Sublacustrine-Fan Mudstones; FDM-W = Fan-Delta Mudstones from the Western slope; FDM-E = Fan-Delta Mudstones from the Eastern slope; SDLM = Semi-Deep Lake Mudstones; SLM = Shallow Lake Mudstones; NSFM = Nearshore Subaqueous Fan Mudstones; Mixed lithology of N + Q = Sandstone (95%) + Conglomerate (5%).



The Qingshui and Chenjia Sags are the primary hydrocarbon-supplying sags to the Xinglongtai structural belt. The primary source rocks in these sags are predominantly characterized by dark mudstone and oil shale in the Es<sub>3</sub> and dark mudstone in the upper section of the Es<sub>4</sub>. These source rocks are composed mainly of a blend of sapropelic and humic organic matter, exhibiting significant heterogeneity. In terms of apparent organic types, the Es<sub>4</sub> source rocks are primarily characterized by types II<sub>1</sub>–I, while Es<sub>3</sub> source rocks are predominantly type II<sub>1</sub> [17–19].

Industrial oil and gas reservoirs identified both inside and outside the buried hills of the Xinglongtai structural belt present differing gas compositions. The gas within the buried hills is thermogenic, encompassing both humic and sapropelic types and primarily originating from Es<sub>3</sub> source rocks. However, the gas outside the buried hills shows a more intricate composition, being a blend of primary microbial gases and thermogenic gases [5–7,17,20].

### 3. Data and Methods

#### 3.1. Database

In this study, we analyzed 204 data points from hydrocarbon source rock samples, including pyrolysis parameters and Total Organic Carbon (TOC). These samples were obtained from sags around the Xinglongtai structural belt (Figure 1). Based on lithofacies classification, the distribution is as follows: 26 Fan-Delta Mudstones from the Western slope (FDM-W), 25 from the eastern slope (FDM-E), 5 Sublacustrine-Fan Mudstones (SFM), 89 Semi-Deep Lake Mudstones (SDLM), 3 Shallow Lake Mudstones (SLM), and 56 Nearshore Subaqueous Fan Mudstones (NSFM) (Table A1). Additionally, we analyzed experimental data from 37 natural gas samples collected at the surface from production wells around the Xinglongtai structural belt in the Western Depression of the Bohai Bay Basin (Figure 1). Of these samples, 25 were from the Ed Fm reservoir, 2 from Es<sub>1</sub>, 2 from Es<sub>3</sub>, and 8 from the basement reservoir. The analysis covered molecular compositions and stable carbon isotope ratios of methane to butane (C<sub>1</sub> to C<sub>5</sub>), as well as carbon dioxide (CO<sub>2</sub>) present in these gas samples (Table A2). The geological data required for basin modeling, including location, formation thickness, fault data, and well logs, are extracted from the 3D seismic survey within the study area. The erosion maps of critical moments are used to determine the erosion thickness at different locations (Table 1). All these data were collected from the Exploration and Development Research Institute of the Liaohe Oilfield.

**Table 1.** Summary of all layers modeled using the PetroMod 2016 software.

Age at the Top (Ma)	Layer Name	PSE	Event Type
0.0	N + Q	Overburden Rock	Deposition
24.6	/	/	Erosion (after Ed)
26.6	Ed	Reservoir Rock	Deposition
36.0	/	/	Erosion (after Es <sub>1+2</sub> )
36.5	Es <sub>1+2</sub>	Reservoir Rock	Deposition
38.0	/	/	Erosion (after Es <sub>3</sub> )
38.3	Es <sub>3</sub> <sup>1</sup>	Rock Source	Deposition
39.0	Es <sub>3</sub> <sup>2</sup>	Source Rock	Deposition
41.5	Es <sub>3</sub> <sup>3</sup>	Source Rock	Deposition
43.0	Es <sub>4</sub> <sup>1</sup>	Source Rock	Deposition
/	Basement	Reservoir Rock	Deposition

Note. Es<sub>3</sub><sup>1</sup>: The upper Submember of the Mbr 3 of the Shahejie Formation. Es<sub>3</sub><sup>2</sup>: The middle Submember of the Mbr 3 of the Shahejie Formation. Es<sub>3</sub><sup>3</sup>: The lower Submember of the Mbr 3 of the Shahejie Formation. Es<sub>4</sub><sup>1</sup>: The upper Submember of the Mbr 4 of the Shahejie Formation.

#### 3.2. Basin Modeling

Basin and Petroleum System Modeling (BPSM) is a crucial discipline in petroleum geology and geophysics. It is extensively employed to forecast and comprehend the occurrence, quantity, and quality of hydrocarbons in subsurface reservoirs [21–24]. Basin and petroleum system modeling integrate various dynamic processes such as sedimentation,

faulting, burial, kerogen maturation kinetics, and multiphase flow. It is an effective tool for analyzing the generation, migration, and accumulation of hydrocarbons [25]. This study selected a representative profile to perform 2D basin modeling using Petromod 2016 software. The specific steps are as follows: (1) Load the extracted stratigraphic and fault data into the model. Age and petroleum system element assignments are shown in Table 2. The study area has experienced three stages of erosion, corresponding to the period after deposition of the Es<sub>3</sub>, Es<sub>1+2</sub>, and Ed. The erosion thickness ranges were 0–200 m, 0–50 m, and 0–200 m, respectively. The maximum erosion thickness is observed at the center of the Xinglongtai structural belt. (2) Each stratigraphic unit was divided into 5 to 15 sublayers based on thickness. The lithofacies were defined based on lithology logs, sedimentary facies distribution, and the 3D geological model established in a previous study [26] for the Western Depression, Liaohe Subbasin (Figure 3). (3) The parameters for the source rocks, including TOC and HI, were set based on the average experimental values of different types of source rocks. The source rocks containing type II kerogen and type III kerogen were assigned to kinetic models from the PetroMod catalog (Burnham, 1989 T-II and Burnham, 1989 T-III), respectively. Maturity was calculated using the EASY %Ro model developed by [27]. (4) The boundary conditions, including paleo-water depth (PWD), paleo-heat flow (PHF), and sediment–water interface temperature (SWIT), were determined based on previous literature. The PWDs for different stratigraphic units were assigned based on their sedimentary facies [28]. The PHF data were from [16]. The SWITs were calculated based on the global mean temperature at sea level for the latitude of 41° in Eastern Asia [29]. (5) The types of faults were determined based on their intersection with the stratigraphic units. The sealing capability of different types of faults was assigned based on the main active periods. During active periods, the faults were open and lasted for 1–2 Ma, while at other times, they were closed. (6) The migration model utilizes the Darcy flow and invasion percolation method.

**Table 2.** Summary of input parameters for Eocene source rocks. The kerogen types were classified following [30], and the hydrocarbon generation kinetic models were proposed by [27].

Formation	TOC (%)	HI (mg HC/g Rock)	Kerogen Type	Kinetic Model
SFM	2.2	305	Type II	(Burnham, 1989 T-II)
FDM-W	1.9	290	Type II	(Burnham, 1989 T-II)
FDM-E	1.5	100	Type III	(Burnham, 1989 T-III)
SDLM	2.2	490	Type I	(Burnham, 1989 T-I)
SLM	1.4	200	Type II	(Burnham, 1989 T-II)
NSFM	1.6	75	Type III	(Burnham, 1989 T-III)

## 4. Results

### 4.1. Natural Gas Geochemistry

#### 4.1.1. Molecular and Carbon Isotopic Composition of Different Alkane Gases

We employ the correlation between molecular and carbon isotopic compositions of alkane gases across varying carbon numbers to identify genetic types and post-generation alterations [10,31,32]. In the Xinglongtai area, the natural gas samples exhibit significant differences in their molecular and carbon isotopic compositions within strata. The basement, Es<sub>4</sub>, Es<sub>3</sub>, and Es<sub>1+2</sub> gas samples display a typical content pattern with  $C_1 \gg C_2 > C_3 > iC_4 < nC_4$  and  $\delta^{13}C_1 < \delta^{13}C_2 < \delta^{13}C_3 > \delta^{13}iC_4 < \delta^{13}nC_4$  ( $\delta^{13}C_3 < \delta^{13}nC_4$ ), indicating the presence of thermogenic gases without observable post-generation alterations [33] (Figure 4). In contrast, the molecular composition of the Ed gas samples exhibits considerably lower levels of wet gases ( $C_{2+}$ ) compared to other gas samples and generally follows an atypical content order of  $C_1 \gg C_2 > C_3 < iC_4 > nC_4$  (Figure 4a). Furthermore, the Ed gas samples display significantly heavier  $\delta^{13}C_3$  and  $\delta^{13}nC_4$  values relative to  $\delta^{13}iC_4$  and, in some cases, exhibit an abnormal ordering of  $\delta^{13}C_3 > \delta^{13}nC_4$  or  $\delta^{13}C_3 < \delta^{13}nC_2$ , suggesting biodegradation (Figure 4b).

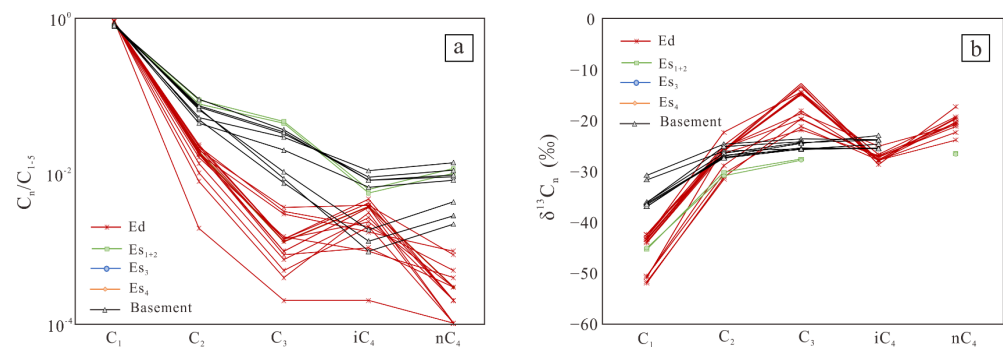


**Figure 4.** (a) Diagrams of  $C_n/C_{1-5}$  ratio and (b) carbon isotope series of natural gas samples from the Xinglongtai area, Liaohe Subbasin, Bohai Bay Basin.

#### 4.1.2. Correlation between $C_1/(C_2 + C_3)$ and $\delta^{13}C_1$

The Bernard diagram, which plots the  $C_1/(C_2 + C_3) - \delta^{13}C_1$  pattern, plays a crucial role in distinguishing microbial gas from thermogenic natural gas derived from different kerogen types. However, due to the heterogeneity of organic sources and secondary processes, variations in chemical and isotopic compositions can introduce uncertainties in genetic classification [10,34,35]. Therefore, it is essential to consider geological evidence, including the structural positioning and connectivity between natural gas reservoirs and sources, and employ multiple parameters or diagrams to make accurate judgments [7,36].

We analyzed natural gas samples from the study area using the  $C_1/(C_2 + C_3) - \delta^{13}C_1$  correlation diagram developed from [34,35] (Figure 5). Analysis showed that samples from the Shahejie Fm and the basement display a consistently low  $C_1/(C_2 + C_3)$  ratio and heavy  $\delta^{13}C_1$ , indicating a thermogenic origin. Upon further classification, three types emerge: gas samples from  $Es_{1+2}$  demonstrate a low  $C_1/(C_2 + C_3)$  ratio ( $<5$ ) and light  $\delta^{13}C_1$  ( $<-39\%$ ), suggesting a sapropelic type; gas samples from the basement present a higher  $C_1/(C_2 + C_3)$  ratio ( $>10$ ) and heavy  $\delta^{13}C_1$  ( $>-34\%$ ), implying a humic type; and gas samples from  $Es_3$  show a high  $C_1/(C_2 + C_3)$  ratio ( $>100$ ) and heavy  $\delta^{13}C_1$  ( $-30\%$ ), suggesting a highly mature humic type. As for gas samples from the Ed, they can be further subdivided based on  $\delta^{13}C_1$  values: samples with  $\delta^{13}C_1 > -45\%$  display a higher  $C_1/(C_2 + C_3)$  ratio ( $>40$ ), indicating significant biodegradation influence; and samples with  $\delta^{13}C_1 < -45\%$  show a higher  $C_1/(C_2 + C_3)$  ratio and reside in a transitional zone, suggesting a potential thermogenic and biodegraded gas mixture (Figure 5).

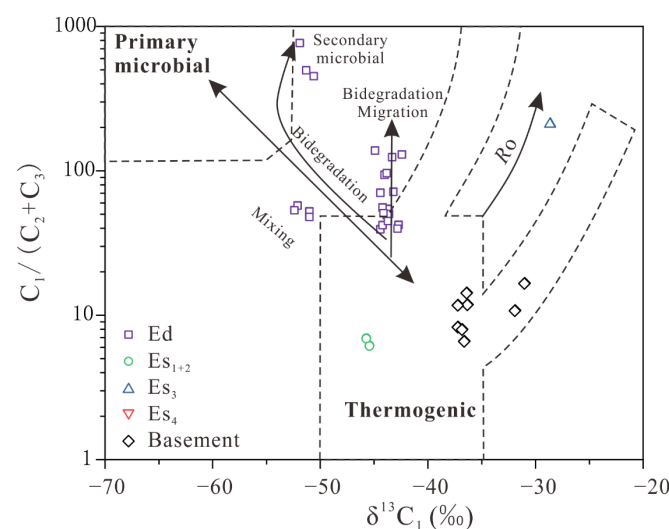


**Figure 5.** Genetic diagram of  $C_1/(C_2 + C_3)$  versus  $\delta^{13}C_1$  for natural gas samples from the Xinglongtai area, Liaohe Subbasin, Bohai Bay Basin. The diagram is modified from [34,35].

#### 4.1.3. Genetic Types of Natural Gas

The carbon isotope composition of natural gas, specifically ethane ( $\delta^{13}\text{C}_2$ ), can indicate the source rock type—either sapropelic or humic [10,31,37–39]. Boundary values, however, remain debated due to varying factors such as the original organic carbon isotope and maturity. Following the approach of [39], we classify  $\delta^{13}\text{C}_2$  values greater than  $-26\text{‰}$  as humic-type gas, less than  $-29\text{‰}$  as oil-type gas, and between  $-29\text{‰}$  and  $-26\text{‰}$  as mixed gas. Normally, propane's carbon isotope ( $\delta^{13}\text{C}_3$ ) also differentiates gas types, but degradation due to microbial activity inhibits its use in this study [40].

The natural gas samples of Ed exhibit a heavier  $\delta^{13}\text{C}_3$ , indicating biodegradation. Some of these gas samples also show a lighter characteristic by  $\delta^{13}\text{C}_1 < -50\text{‰}$ , possibly due to mixing with biodegraded thermogenic gases, while others are likely secondary microbial gases. The natural gas samples from Es<sub>1+2</sub> are characterized by  $\delta^{13}\text{C}_2 > -28\text{‰}$ , indicating sapropelic-type gases. On the contrary, the natural gas samples from Es<sub>3</sub> are characterized by  $\delta^{13}\text{C}_2 < -28\text{‰}$ , indicating humic-type gases. Samples from the basement are predominantly mixed gases (mixed humic and sapropelic gas), with a minor proportion of humic-type gases (Figure 6).

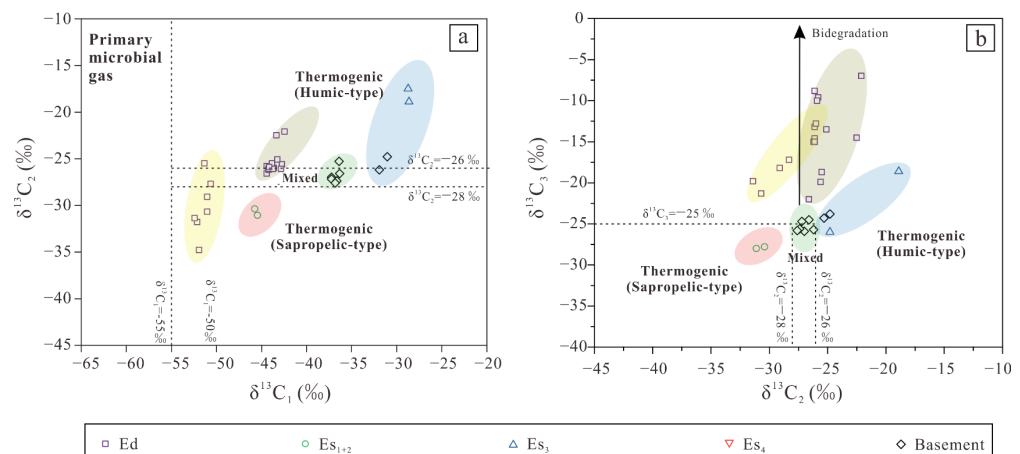


**Figure 6.** (a) Cross plot of  $\delta^{13}\text{C}_1$  versus  $\delta^{13}\text{C}_2$  and (b)  $\delta^{13}\text{C}_2$  versus  $\delta^{13}\text{C}_3$  for natural gas samples from the Xinglongtai area, Liaohe Subbasin, Bohai Bay Basin.

#### 4.2. Source Rock Types and Assessment

Considering the variations in organic matter sources and preservation conditions, mudstones formed in different depositions can manifest a wide range of geochemical properties. This is particularly evident in lacustrine basins with substantial tectonic evolution and changes in sedimentary systems [41,42]. Within the Shahejie Fm, known for its deltaic–lacustrine and lacustrine–turbidite depositional environments [9,16,43–46], we have identified six potential source rock types: Sublacustrine-Fan Mudstones (SFM), Fan-Delta Mudstones from the Western slope (FDM-W), Fan-Delta Mudstones from the Eastern slope (FDM-E), Semi-Deep Lake Mudstones (SDLM), Shallow Lake Mudstones (SLM), and Nearshore Subaqueous Fan Mudstones (NSFM).

##### 4.2.1. Organic Matter Richness

The TOC content of SDLM ranges predominantly between 2.45% and 4.30%, averaging 3.4%. Their hydrocarbon generation potential ( $S_1 + S_2$ ), plotted against TOC, suggests these are good to excellent source rocks. SLM have the next-highest TOC content, mainly ranging from 0.75% to 1.80%, with an average of 1.35%, and are classified as poor to good source rocks based on hydrocarbon generation potential. The TOC values for all other mudstone types exceed 1%, indicating medium to good hydrocarbon generation potential. Hence, the organic matter abundance in the study area generally meets the lower limit (TOC = 0.5%) for hydrocarbon generation (Figure 7a,b).



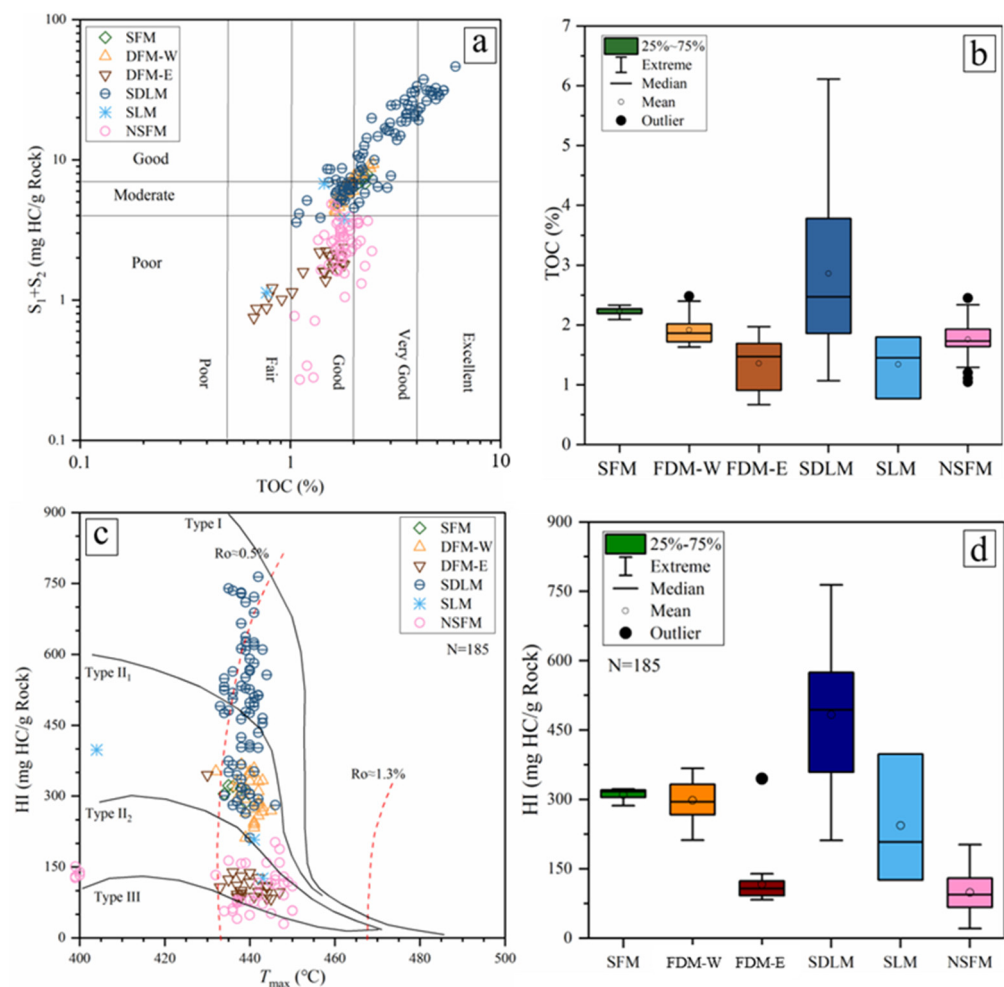


**Figure 7.** (a) Cross-plot of TOC versus ( $S_1 + S_2$ ) [47]. (b) Box plot of mudstone types and TOC contents. (c) Cross-plot of HI versus  $T_{max}$  of mudstones. (d) Box plot of mudstone types and HI contents.

#### 4.2.2. Kerogen Type

The source rock samples from the study area encompass a variety of organic matter types. Contributions from sapropelic, mixed sapropelic–humic, and humic organic matter are evident and correlate with source rock types. SDLM primarily contain type I–II<sub>1</sub> organic matter. FDM developed on the Western slope (FDM-W) and SFM mainly possess type II<sub>1</sub>–II<sub>2</sub> organic matter. SLM are of type II<sub>2</sub> organic matter, while the FDM on the Eastern slope (FDM-E) and NSF primarily contain type III organic matter (Figure 7c). According to box plots in Figure 7b–d, the average values of TOC and HI for different types of source rocks have been calculated (Table 2). The results are used as input parameters in basin modeling.

### 4.3. Modeling of Gas Generation, Migration, and Accumulation

#### 4.3.1. Hydrocarbon Generation History

We selected a representative profile for 2D basin modeling to reconstruct the dynamic history of hydrocarbon generation in the study area. The Transformation Ratio (TR), typically corresponding to the maturity of the source rocks, is commonly used to denote the timing of hydrocarbon generation and expulsion [48]. Based on the hydrocarbon generation process proposed by [48], the results reveal the following: (1) At 40 Ma, only  $Es_4^1$  and lower  $Es_3^3$  source rocks in the central Qingshui Sag entered the oil generation window ( $R_o > 0.5\%$ ) (Figure 8a,b). Meanwhile, the source rocks in the Chenjia Sag had not reached

the mature stage due to their relatively shallow burial depth. (2) By 38 Ma,  $Es_4^1$  and part of  $Es_3^3$  in the Qingshui Sag had entered the gas generation stage ( $Ro > 1.3\%$ ) due to deep burial. The upper part of  $Es_3^3$  to the lower part of  $Es_3^2$  was in peak oil generation, with a TR of 40–60%. A small segment of  $Es_4^1$  in the western slope entered the oil generation stage, with a maximum TR exceeding 50% (Figure 8c,d). In the Chenjia Sag, the source rocks of  $Es_4^1$ ,  $Es_3^3$ , and the bottom of  $Es_3^2$  entered the oil window, with TR ranging from 20% to 50%. (3) At 30 Ma, the  $Es_4^1$ ,  $Es_3^3$ , and part of the  $Es_3^2$  in the central Qingshui Sag entered the main gas generation stage ( $Ro > 1.3\%$ ), with a significant strata thickness reaching the dry gas generation stage ( $Ro > 2.0\%$ ). By contrast, only the  $Es_4^1$  source rocks reached the gas window in the Chenjia Sag. During this stage, except for the western slope belt at the basin margin, all formations of the Shahejie Fm in the study area had entered the oil window, with the maximum TR reaching 100% (Figure 8e,f). Due to the diverse types of organic matter present in the source rocks, the TR of these rocks at the same depth may vary. (4) During 30–0 Ma, the Liaohe Subbasin became relatively stable, and hydrocarbon generation almost ceased (Figure 8g,h).

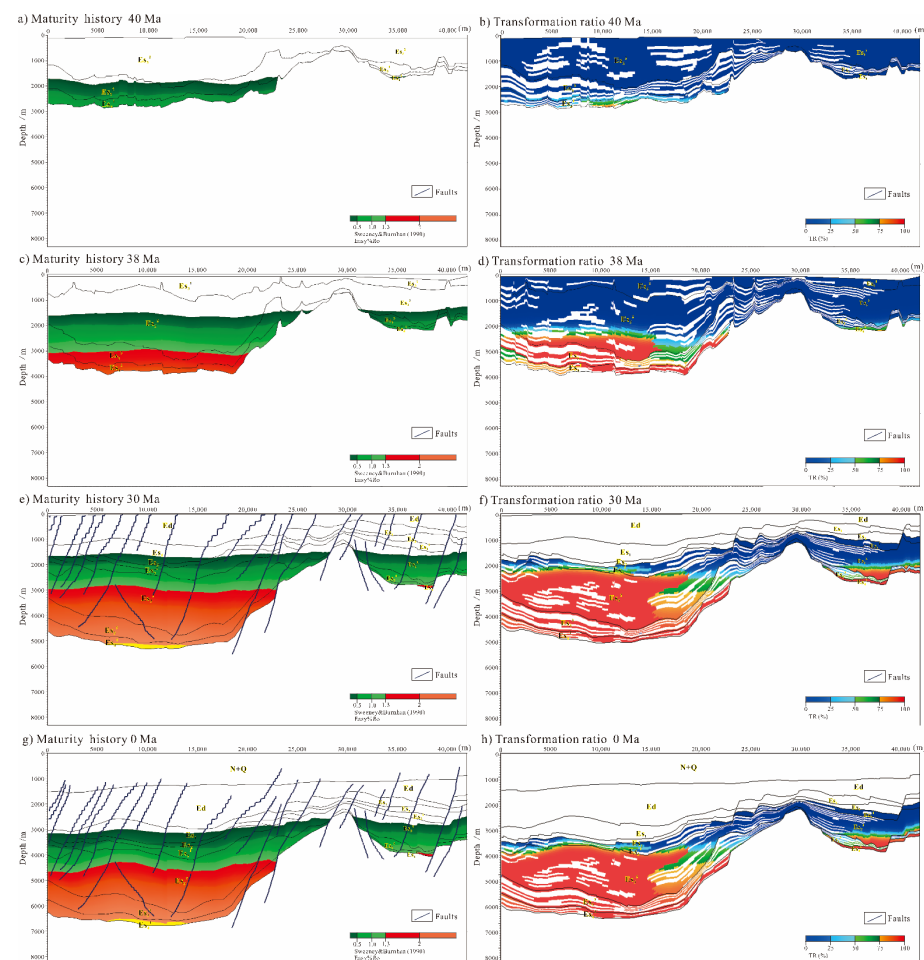


**Figure 8.** Evolution of the maturity and the transformation ratio with age in Profile AA' at 40 Ma (a,b), 38 Ma (c,d), 30 Ma (e,f), and 0 Ma (g,h).

By assessing the volume changes in natural gas generated by source rocks from each unit along the AA' cross-section over geological time, we can divide the entire process into a single hydrocarbon generation phase from 40 Ma to 34 Ma. Both  $Es_4^1$  and  $Es_3^3$  commenced gas generation concurrently.  $Es_3^2$  had the longest gas generation period, attributable to its maximum shale thickness, whereas  $Es_3^3$  had the latest onset of gas generation (Figure 9).

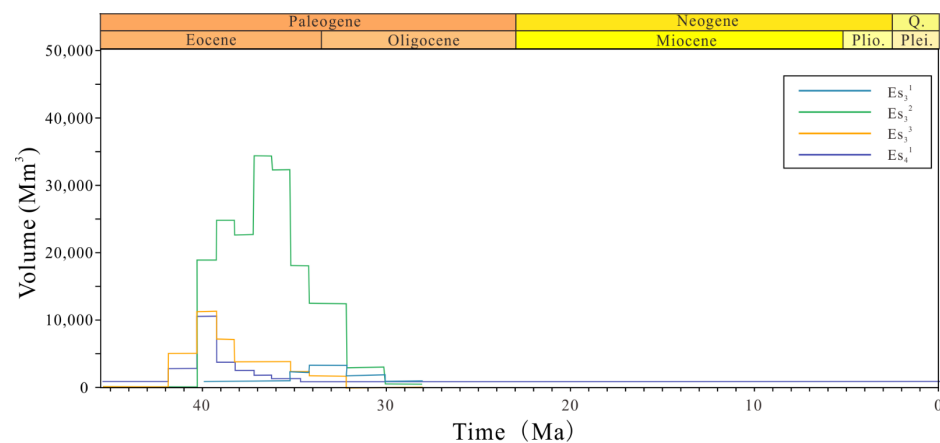


**Figure 9.** Diagrams showing the gas generation with time in Profile AA'.

#### 4.3.2. Gas Migration and Accumulation History

As demonstrated in Figure 10, simulation results of natural gas migration and accumulation suggest reservoirs are found both within (basement) and outside ( $Es_{1+2}$ ,  $Es_3$ , and Ed) the buried hill of the Xinglongtai structural belt. This distribution aligns well with the actual exploration results of natural gas reservoirs. The simulation successfully predicted the existing natural gas reservoirs extracted from wells MN603, MT1, M256, and X256-2.

The history of natural gas migration and accumulation in the study area can be summarized as follows: (1) Beginning at 40 Ma, natural gas generated in the Qingshui Sag began to migrate upward, while the Chenjia Sag showed a relatively lower production of natural gas (Figure 10a). By 38 Ma, in situ structural natural gas reservoirs began to form within  $Es_3$  in both sags, attributed to the absence of fault conduction during this period. Meanwhile, the natural gas generated from  $Es_4$  underwent lateral migration and accumulation in the cracks inside the Xinglongtai buried hill (Figure 10b). (2) Around 34 Ma, concurrent with the Ed deposition period, most faults became active. These primarily included the syndepositional faults between the Qingshui Sag and the Xinglongtai structural belt, as well as other faults intersecting the  $Es_3$  and Ed. At this time, these faults served as conduits, directing the natural gas produced within the central sags towards the sand bodies present in  $Es_{1+2}$ – $Es_3$  of the Xinglongtai structural belt (Figure 10b,c). (3) After 30 Ma, as the basin deepened, fault displacement increased, and the formation of fault mud drapes contributed to the occurrence of natural gas reservoirs along these faults (Figure 10c,d).

#### 4.3.3. Contribution of Source Rocks in the Filling of Reservoirs

Furthermore, according to the migration simulation results of Profile AA', we calculated the contribution ratios of gas source rocks to various representative gas reservoirs over time. The in situ and basement natural gas reservoirs, once established in the early stages, did not undergo any secondary transformations. The  $Es_3$  natural gas reservoirs located within the Qingshui and Chenjia Sags were primarily contributed by the Nearshore Subaqueous Fan Mudstones (NSFM—Type III organic matter) of their respective  $Es_3$  layers. Meanwhile, the anticlinal natural gas reservoirs within the Xinglongtai structural belt received a mixture of contributions from the Shallow Lake Mudstones (SLM—Type II organic matter) from the  $Es_4$  layer of the Qingshui Sag and the NSFM from the  $Es_3$  layer of the Chenjia Sag (Figure 11). Reservoirs outside the Xinglongtai buried hill, which formed later, received their  $Es_{1+2}$  natural gas primarily from the Semi-Deep Lake Mudstones (SDLM—Type I organic matter) of the  $Es_3$  layer from the Qingshui Sag. The  $Es_3$  natural gas was primarily contributed by the NSFM from the  $Es_3$  layers in both sags (Figure 11b,c).

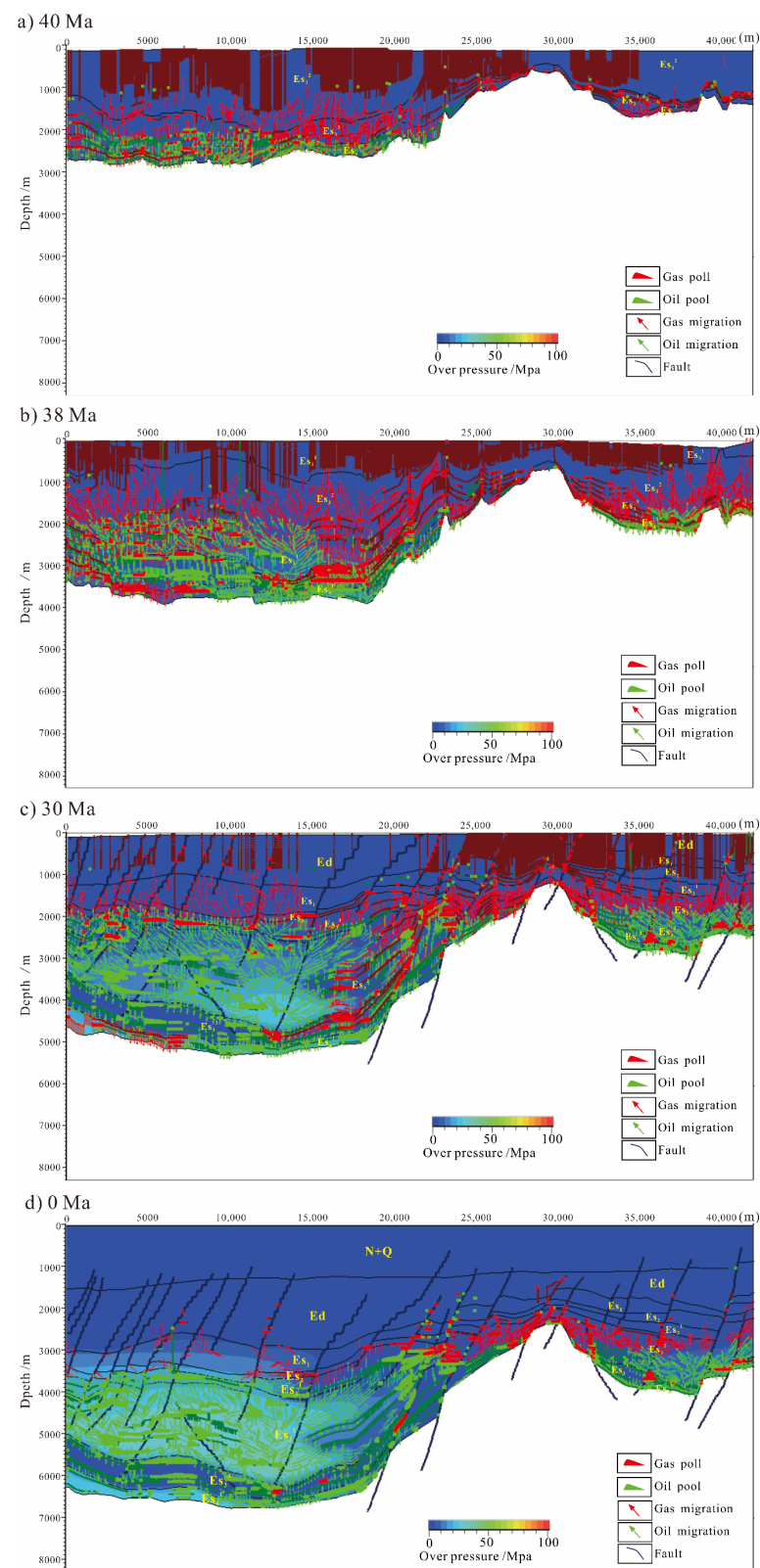


**Figure 10.** Simulation results of hydrocarbon migration and accumulation in Profile CC' at 40 Ma (a), 38 Ma (b), 30 Ma (c), and 0 Ma (d). Under the background of overpressure.



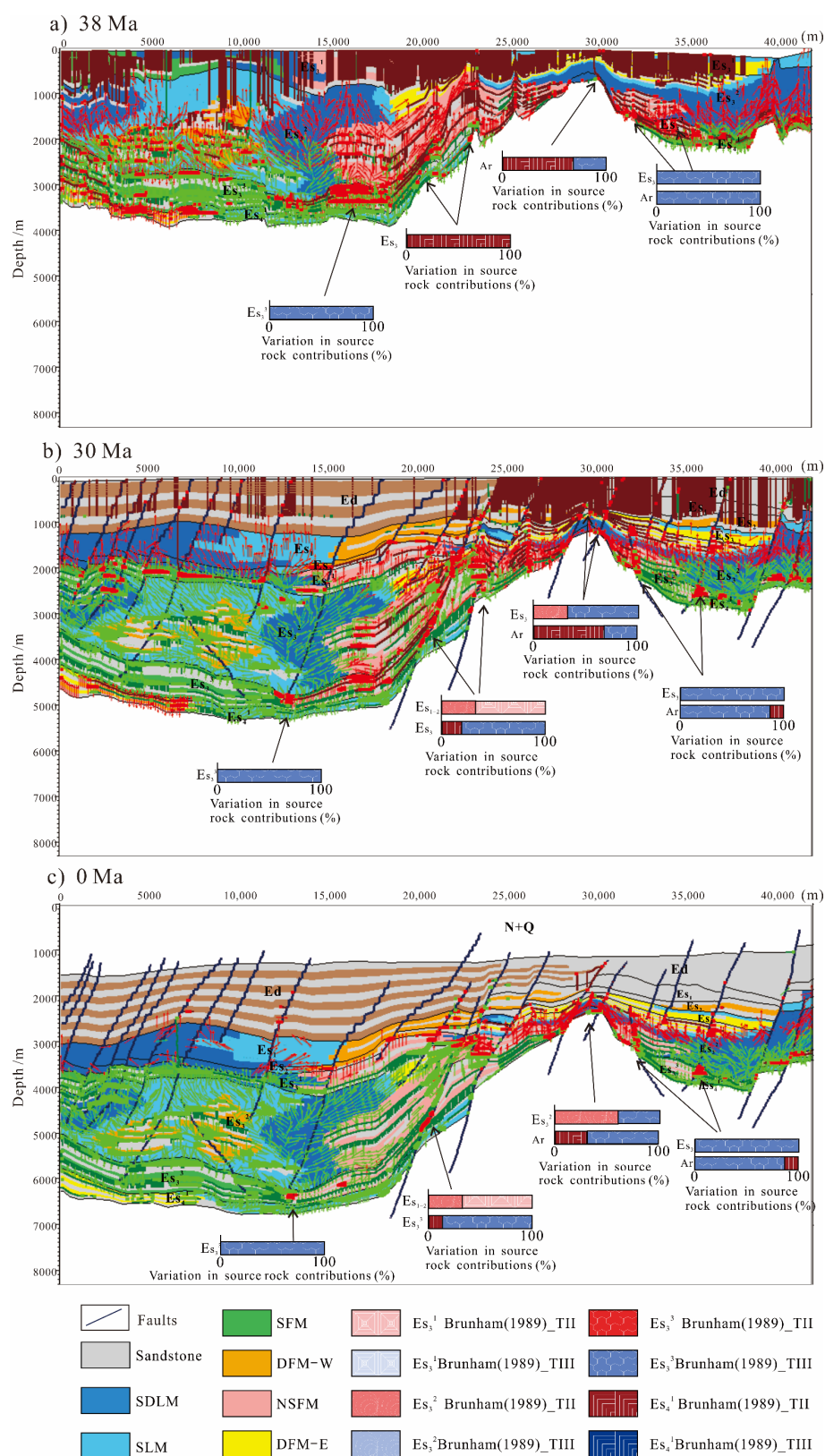


**Figure 11.** Simulation results of hydrocarbon accumulation and proportional contribution of source rocks in each stratum in Profile CC' at 38 Ma (a), 30 Ma (b), and 0 Ma (c).

## 5. Discussion

### 5.1. Source of Thermogenic Gas

Oil and gas generation from sapropelic organic matter are intertwined, with oil generation taking precedence during the mature stage. Conversely, humic organic matter primarily generates a minimal amount of light oil in the mature stage, while gas generation is the dominant process throughout the entire maturation cycle [18,48]. According to the findings in Section 4.2, there is a distinct correlation between the type of organic matter in source rocks and the categorization of those rocks. NSFm and FDM-E are mainly contributed by Type III organic matter, which generates humic-type gas throughout the maturity process. In contrast, the remaining mudstone types (FDM-W, SLM, and SDLm) primarily consist of Type I-II organic matter, which largely produces sapropelic-type gas at the high maturity stage.

Given the poor connectivity of reservoir fractures inside the buried hill, it is not conducive to the migration of natural gas within it. As a result, the source rock of the natural gas is in direct contact with the buried hill [6]. Based on the distribution of different types of source rocks in the profile (Figure 3), those in direct contact with the Xinglongtai buried hill are SLM in Es<sub>4</sub> and NSFm in Es<sub>3</sub>, which generate sapropelic-type gas and humic-type gas, respectively. Therefore, the humic-type gas found inside the Xinglongtai buried hill is contributed by the NSFm in Es<sub>3</sub>, and the mixed gas (a combination of sapropelic-type gas and humic-type gas) is contributed by both the SLM in Es<sub>4</sub> and the NSFm in Es<sub>3</sub>. These findings are in line with the results of the source–reservoir–accumulation simulation for gas origin comparison (Figure 11).

The SDLm and SLM in the Es<sub>3</sub><sup>2</sup> of the Qingshui Sag have entered the gas-generating stage ( $R_o > 2.0\%$ ), thereby generating sapropelic-type gas. This indicates that these source rocks may serve as the primary contributors to the sapropelic-type gas found in the Es<sub>1+2</sub> of the Xinglongtai structural belt. Meanwhile, the humic-type gas in Es<sub>3</sub> originates from the NSFm within the Es<sub>3</sub>.

### 5.2. Petroleum System

We have delineated the important elements of the petroleum systems both inside and outside the Xinglongtai structural belt (Figure 12). The main source rocks external to Xinglongtai are the Es<sub>4</sub> and Es<sub>3</sub> shales, with the reservoir rocks being the Es<sub>3</sub>, Es<sub>1+2</sub>, and Ed sandstones and the cap rock being the Ed shale. The generation of natural gas spanned from the middle Eocene to the early Oligocene period. The migration of natural gas is jointly dictated by hydrocarbon generation and the associated fracture systems. Importantly, faults activated during the Oligocene period restructured the deep natural gas reservoirs that were formed earlier, leading to secondary migration and accumulation of natural gas. As such, the crucial period for the system outside Xinglongtai transpired during the Oligocene period. Within the confines of Xinglongtai, the principal source rocks are also the Es<sub>4</sub> and Es<sub>3</sub> shales, with the natural gas stored in the basal fractures and the cap rock being the Es shale. The generation of natural gas likewise occurred from the middle Eocene to the early Oligocene period. The migration of natural gas is co-governed by hydrocarbon generation and fractures in rocks below the unconformity. Consequently, the critical moment for the system within Xinglongtai occurred in the mid-Eocene period.

### 5.3. Implications for Natural Gas Accumulation

This study categorizes the Xinglongtai area into two distinct hydrocarbon accumulation systems: the inner and outer Xinglongtai buried hill systems.

The inner Xinglongtai buried hill system receives contributions from two source directions, namely the Qingshui and Chenjia Sags. The Nearshore Subaqueous Fan Mudstones (predominantly composed of humus organic matter) and Semi-Deep Lake Mudstones (mainly constituting sapropelic organic matter) within the Es<sub>3</sub> sag generate humic-type gas and oil-type gas, respectively, under thermal influence. These gases accumulate in the Es<sub>3</sub> and Es<sub>1+2</sub> layers. As the burial depth decreases to less than 2000 m, the system enters a

transitional stage between thermal and biological influences, with the thermogenic natural gas either biodegraded or further mixed with primary biogas. The primary migration and accumulation routes are dictated by faults, with long-distance vertical migration being the most prevalent. Due to two instances of fault activity, the system underwent two migration phases, with the present natural gas reservoir formed after the Oligocene fault activity and preserved until now (Figure 13a,c).

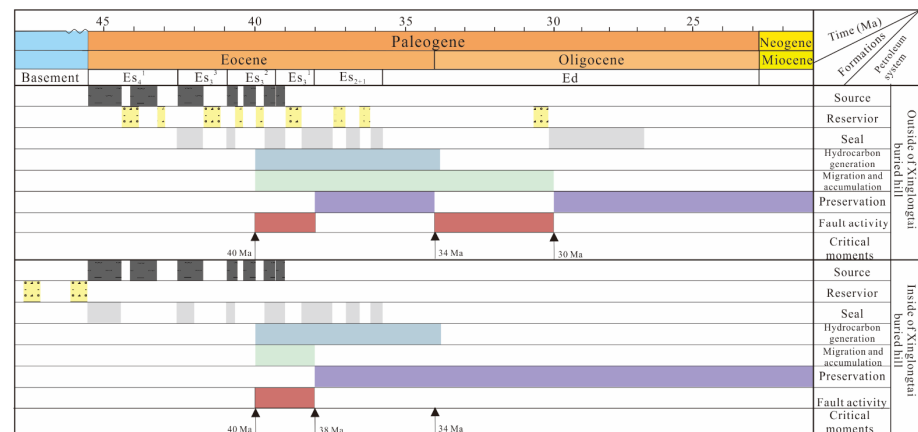


**Figure 12.** Events chart showing the petroleum system elements in the Xinglongtai structural belt.

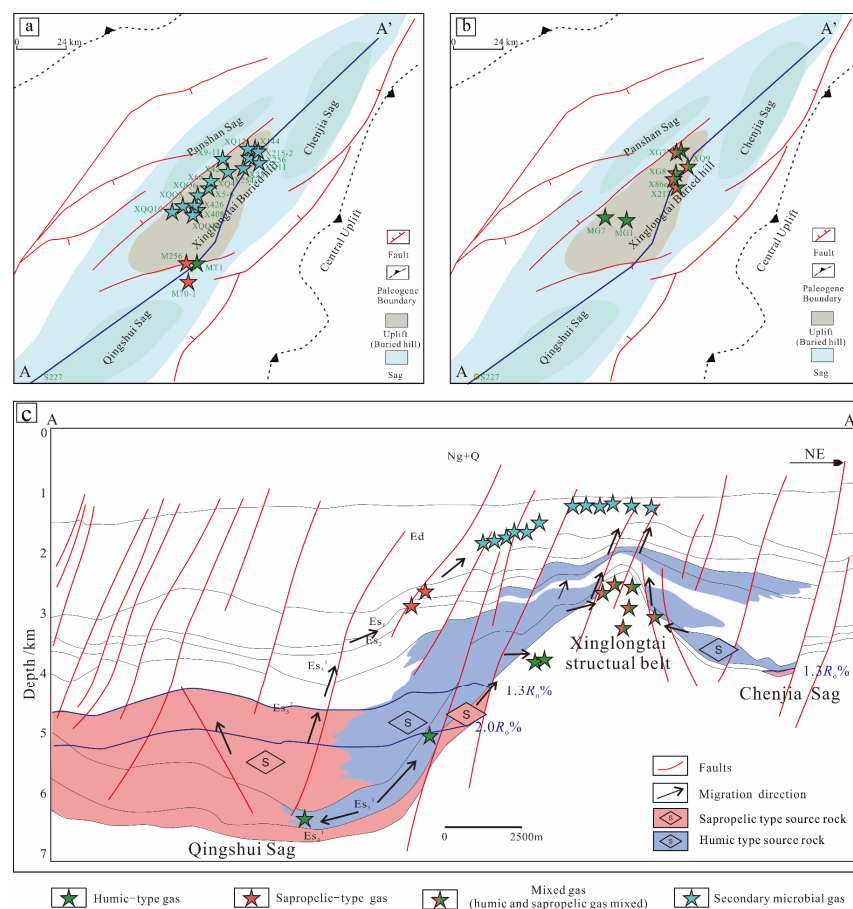


**Figure 13.** (a) Genetic types of gas samples in the outer Xinglongtai buried hill; (b) genetic types of gas samples in the inner Xinglongtai buried hill; (c) origin and accumulation of natural gases in the Xinglongtai structural belt, Western Depression.

The outer Xinglongtai buried hill system also draws from two source directions in the Qingshui and Chenjia Sags. However, the sources are the Nearshore Subaqueous Fan Mudstones of Es<sub>3</sub> and the Shallow Lake Mudstones of Es<sub>4</sub> (primarily contributed by sapropelic organic matter) from the Qingshui and Chenjia Sags, which generate coal-type gas and sapropelic-type gas, respectively, under thermal influence. The natural fractures are the principal transmission system [2], and the fractures in the basement constitute the reservoir, so the system experienced only a single phase of migration and accumulation during the Eocene period. Sapropelic-type gas and coal-type gas mingle within the unconformity surface and reservoir to form mixed natural gas reservoirs (Figure 13b,c).

#### 5.4. Significance

Terrestrial lacustrine basins typically exhibit a relatively enclosed structural environment, leading to hydrocarbons often accumulating within or near hydrocarbon-generating sags. Given this context, the distribution and properties of source rocks play a significant role in determining the distribution and characteristics of oil and gas.

The presence of diverse fault systems within faulted lacustrine basins can result in a heterogeneous distribution of source rocks. This, in turn, adds complexity to the distribution of natural gas reservoirs, which often manifest as more abundant accumulations near the hydrocarbon-generating sags. As a result, natural gas reservoirs in the Xinglongtai structural belt are generally richer and deeper. Additionally, the geochemical attributes of the source rocks, such as organic matter type, abundance, and maturity, also exhibit heterogeneity in these faulted lacustrine basins. Variations in organic matter type and maturity influence the genesis type of natural gas that source rocks generate, and the organic matter's abundance impacts the hydrocarbon-generating capability of the source rocks. This leads to multiple genesis types of natural gas coexisting within the same terrestrial lacustrine basin. Moreover, complex fault systems play a pivotal role in natural gas transmission within these basins. The distribution of these faults, coupled with their multiple periods of activity, can spur natural gas migration or diffusion and can potentially disrupt early gas reservoirs. This promotes further mixing of different genesis types of natural gas during migration and diffusion processes.

Consequently, by elucidating the heterogeneity of source rocks—their distribution, organic matter type, abundance, and maturity—and their relationship with the distribution and genesis type of natural gas, along with analyzing the dynamic processes of generation, migration, and accumulation, we can enhance our understanding and prediction of natural gas distribution and storage patterns in terrestrial faulted lacustrine basins. This insight could guide and inform decision-making processes for natural gas exploration and development.

## 6. Conclusions

In conclusions, our study provides insightful revelations on the complex systems governing the generation, migration, and accumulation of natural gas in terrestrial faulted lacustrine basins. These findings can be drawn as follows:

1. Within the peripheries of the Xinglongtai structural belt, in the Qingshui and Chenjia Sags, the primary hydrocarbon source beds are the Es<sub>4</sub> and Es<sub>3</sub> of the Shahejie Fm; Es<sub>4</sub> is characterized by Shallow Lake Mudstones (SLM) and dominated by type II organic matter, while Es<sub>3</sub> mainly comprises Nearshore Subaqueous Fan Mudstones (NSFM) and Semi-Deep Lake Mudstones (SDLM), primarily contributed by type III and type I organic matter, respectively. These factors play a critical role in determining the genesis type of natural gas and the hydrocarbon-generating capacity of the source rocks.
2. The distribution of varied source rocks has a direct bearing on the type of gas discovered within different layers and positions. Inside the Xinglongtai structural belt, the natural gas comprises humic-type and mixed-type gas (a blend of sapropelic and humic-type gases) originating from Es<sub>3</sub> NSFM and Es<sub>4</sub> SLM. Outside the Xinglongtai



structural belt, the natural gas encompasses sapropelic-type gas, humic-type gas, and secondary biodegraded gas. The humic gas derives from Es<sub>3</sub> Nearshore Subaqueous Fan Mudstones, whereas the sapropelic gas stems from Es<sub>3</sub> SDLM.

3. The Xinglongtai structural belt hosts two distinct hydrocarbon accumulation systems, one outside and one inside the buried hill. For the system outside the buried hill, the migration and accumulation of natural gas are guided by a complex fault system within the lacustrine basin. Two separate periods of fault activity not only encouraged the vertical migration and diffusion of natural gas but also disrupted early gas reservoirs, leading to a later-stage consolidation of the natural gas. This system exhibits dual-source directions, dual-source rock types, two migration phases, and late-stage accumulation. Contrastingly, within the buried hill system, the reservoirs nested in the basement are primarily steered by hydrocarbon generation. The further mixing of various genesis types of natural gas within the unconformities and fractures culminates in early-stage accumulation. This system presents dual-source directions, dual-source rock types, a single migration phase, and early-stage accumulation.

**Author Contributions:** S.Y.: provided ideas, wrote, reviewed, and edited the manuscript; M.L. and H.X.: revised the manuscript; S.H., Y.W. and W.K.: collected data and materials; F.W.: analyzed data. All authors have read and agreed to the published version of the manuscript.

**Funding:** This work was funded by the National Natural Science Foundation of China (Grant No. 42173054) and the Natural Science Foundation of Sichuan Province (No. 2022NSFSC0182).

**Data Availability Statement:** Data will be made available on request.

**Acknowledgments:** This work was partly supported by the CNPC Liaohe Oilfield Exploration and Development Company for data support and for making an academic license available for the use of PetroMod.

**Conflicts of Interest:** The authors declare no conflict of interest.

## Appendix A

**Table A1.** Hydrogen index (HI), pyrolysis parameters of all mudstone samples.

Sample ID	Depth (m)	Strata	Mudstone Types	TOC (%)	Pyrolysis Data		
					S <sub>1</sub> (mg/g)	S <sub>2</sub> (mg/g)	T <sub>max</sub> (°C)
SG1-1	3239	Es <sub>3</sub>	FDM-W	1.99	0.71	6.34	437
SG1-2	3372	Es <sub>3</sub>	FDM-W	1.87	0.84	5.49	439
SG1-3	3518	Es <sub>3</sub>	FDM-W	2.21	0.7	7.33	440
SG1-4	3537	Es <sub>3</sub>	FDM-W	2.40	0.78	7.95	442
SG1-5	3752	Es <sub>3</sub>	FDM-W	1.72	1.12	4.02	441
SG1-6	3819	Es <sub>3</sub>	FDM-W	1.64	0.78	3.48	439
SG1-7	2906	Es <sub>3</sub>	FDM-W	2.02	0.35	7.12	432
SG1-8	3464	Es <sub>3</sub>	FDM-W	1.8	0.33	5.99	437
SG1-9	3516	Es <sub>3</sub>	FDM-W	2.22	0.48	7.4	443
SG1-10	3518	Es <sub>3</sub>	FDM-W	2.01	0.52	7.21	441
SG1-11	3520	Es <sub>3</sub>	FDM-W	1.86	0.27	5.5	437
SG1-12	3534	Es <sub>3</sub>	FDM-W	2.38	0.42	8.74	438
SG1-13	3536	Es <sub>3</sub>	FDM-W	2.11	0.5	7.42	440
SG1-14	3538	Es <sub>3</sub>	FDM-W	2.48	0.74	8.6	440
SG1-15	3620	Es <sub>3</sub>	FDM-W	1.82	0.68	5.65	442
SG1-16	3622	Es <sub>3</sub>	FDM-W	1.87	0.83	5.9	439
SG1-17	3680	Es <sub>3</sub>	FDM-W	1.63	0.55	4.67	442
SG1-18	3686	Es <sub>3</sub>	FDM-W	1.99	0.56	5.44	441
SG1-19	3692	Es <sub>3</sub>	FDM-W	1.63	0.59	4.32	439
SG1-20	3696	Es <sub>3</sub>	FDM-W	1.72	0.44	4.59	443

Table A1. Cont.

Sample ID	Depth (m)	Strata	Mudstone Types	TOC (%)	Pyrolysis Data		
					S <sub>1</sub> (mg/g)	S <sub>2</sub> (mg/g)	T <sub>max</sub> (°C)
SG1-21	3704	Es <sub>3</sub>	FDM-W	1.71	0.41	4.61	445
SG1-22	3710	Es <sub>3</sub>	FDM-W	1.75	0.64	4.92	442
SG1-23	3712	Es <sub>3</sub>	FDM-W	1.71	0.44	4.19	441
SG1-24	3722	Es <sub>3</sub>	FDM-W	1.91	0.58	5.27	443
SG1-25	3728	Es <sub>3</sub>	FDM-W	1.77	0.3	4.58	442
SG1-26	3732	Es <sub>3</sub>	FDM-W	1.63	0.47	3.92	441
SG1-27	4280	Es <sub>4</sub>	FDM-E	0.79	0.07	1	442
SG1-28	4282	Es <sub>4</sub>	FDM-E	0.67	0.03	0.72	444
SG1-29	4284	Es <sub>4</sub>	FDM-E	0.77	0.04	0.84	444
SG1-30	4286	Es <sub>4</sub>	FDM-E	0.69	0.06	0.81	440
SG1-31	4288	Es <sub>4</sub>	FDM-E	0.91	0.13	0.88	447
SG1-32	4290	Es <sub>4</sub>	FDM-E	1.97	0.06	6.79	430
SG1-33	4292	Es <sub>4</sub>	FDM-E	1.81	0.36	2	444
SG1-34	4292	Es <sub>4</sub>	FDM-E	1.66	0.36	2	444
SG1-35	4294	Es <sub>4</sub>	FDM-E	1.8	0.21	1.58	438
SG1-36	4296	Es <sub>4</sub>	FDM-E	1.38	0.4	1.8	438
SG1-37	4298	Es <sub>4</sub>	FDM-E	1.15	0.17	1.42	435
SG1-38	4300	Es <sub>4</sub>	FDM-E	0.82	0.08	1.14	436
SG1-39	4300	Es <sub>4</sub>	FDM-E	0.82	0.52	1.86	431
SG1-40	4302	Es <sub>4</sub>	FDM-E	1.02	0.12	1.02	438
SG1-41	4304	Es <sub>4</sub>	FDM-E	1.77	0.29	1.53	437
SG1-42	4306	Es <sub>4</sub>	FDM-E	1.64	0.31	1.82	437
SG1-43	4308	Es <sub>4</sub>	FDM-E	1.74	0.36	1.65	444
SG1-44	4310	Es <sub>4</sub>	FDM-E	1.59	0.3	1.56	442
SG1-45	4312	Es <sub>4</sub>	FDM-E	1.55	0.41	1.66	433
SG1-46	4314	Es <sub>4</sub>	FDM-E	1.69	0.25	1.41	444
SG1-47	4316	Es <sub>4</sub>	FDM-E	1.59	0.32	1.39	441
SG1-48	4318	Es <sub>4</sub>	FDM-E	1.44	0.24	1.36	438
SG1-49	4320	Es <sub>4</sub>	FDM-E	1.47	0.16	1.22	445
SG1-50	4322	Es <sub>4</sub>	FDM-E	1.46	0.24	1.34	437
SG1-51	4328	Es <sub>4</sub>	FDM-E	1.48	0.19	2.04	440
S213-1	3440	Es <sub>3</sub>	SDLM	1.2	0.23	4.9	440
S213-2	3442	Es <sub>3</sub>	SDLM	1.77	0.15	5.1	437
S213-3	3450	Es <sub>3</sub>	SDLM	1.39	0.2	3.66	439
S213-4	3458	Es <sub>3</sub>	SDLM	1.99	0.24	6.07	440
S213-5	3464	Es <sub>3</sub>	SDLM	1.86	0.22	5.92	438
S213-6	3472	Es <sub>3</sub>	SDLM	1.75	0.26	4.9	441
S213-7	3486	Es <sub>3</sub>	SDLM	1.64	0.2	5.5	438
S213-8	3488	Es <sub>3</sub>	SDLM	2.14	0.26	6.51	440
S213-9	3496	Es <sub>3</sub>	SDLM	1.92	0.3	5.39	446
S213-10	3504	Es <sub>3</sub>	SDLM	1.89	0.75	5.31	436
S213-11	3524	Es <sub>3</sub>	SDLM	1.77	0.25	6.23	441
S213-12	3526	Es <sub>3</sub>	SDLM	2.9	0.19	6.14	440
S213-13	3554	Es <sub>3</sub>	SDLM	1.72	0.23	5.92	437
S213-14	3558	Es <sub>3</sub>	SDLM	2.26	0.45	6.81	438
S213-15	3568	Es <sub>3</sub>	SDLM	1.89	0.71	5.55	442
S213-16	3574	Es <sub>3</sub>	SDLM	1.74	0.35	4.78	438
S213-17	3582	Es <sub>3</sub>	SDLM	2	0.56	6.28	439
Q233-1	3451	Es <sub>3</sub>	SFM	2.09	0.35	6.37	434
Q233-2	3352.25	Es <sub>3</sub>	SFM	2.27	0.28	6.5	439
Q233-3	3352.75	Es <sub>3</sub>	SFM	2.27	0.41	7.19	438
Q233-4	3353.25	Es <sub>3</sub>	SFM	2.33	0.37	7.47	436
Q233-5	3353.75	Es <sub>3</sub>	SFM	2.19	0.32	7.06	435
D306-1	3373	Es <sub>3</sub>	SLM	0.77	0.16	0.97	443
D306-2	3413	Es <sub>3</sub>	SLM	1.45	1	5.77	404
D306-3	3414	Es <sub>3</sub>	SLM	1.8	0.07	3.74	441

Table A1. Cont.

Sample ID	Depth (m)	Strata	Mudstone Types	TOC (%)	Pyrolysis Data		
					S <sub>1</sub> (mg/g)	S <sub>2</sub> (mg/g)	T <sub>max</sub> (°C)
SG168-1	2913	Es <sub>3</sub>	SDLM	3.56	1.37	17.45	433
SG168-2	2919	Es <sub>4</sub>	SDLM	3.37	0.81	17.95	438
SG168-3	2925	Es <sub>4</sub>	SDLM	5.38	3.45	27.9	436
SG168-4	2931	Es <sub>4</sub>	SDLM	4.46	1.88	24.46	434
SG168-5	2937	Es <sub>4</sub>	SDLM	5.36	3.08	28.1	434
SG168-6	2955	Es <sub>4</sub>	SDLM	4.93	2.38	30.06	443
SG168-7	2961	Es <sub>4</sub>	SDLM	4.61	2.35	28.79	441
SG168-8	2967	Es <sub>4</sub>	SDLM	4.62	2.44	28.62	441
SG168-9	2973	Es <sub>4</sub>	SDLM	6.11	4.18	42.04	441
SG168-10	2979	Es <sub>4</sub>	SDLM	4.46	4.07	27.3	438
SG168-11	2985	Es <sub>4</sub>	SDLM	3.5	3.6	23.28	438
SG168-12	2991	Es <sub>4</sub>	SDLM	4.31	5.8	31.66	436
SG168-13	2997	Es <sub>4</sub>	SDLM	4	3.88	29.58	435
SG168-14	3003	Es <sub>4</sub>	SDLM	3.92	2.68	27.84	439
SG168-15	3009	Es <sub>4</sub>	SDLM	3.18	1.76	22.94	441
SG168-16	3015	Es <sub>4</sub>	SDLM	2.44	2.01	17.82	438
SG168-17	3021	Es <sub>4</sub>	SDLM	3.02	2.48	22	438
SG168-18	3027	Es <sub>4</sub>	SDLM	2.96	1.85	14.24	435
SG168-19	3033	Es <sub>4</sub>	SDLM	3.62	2.67	22.04	439
SG168-20	3039	Es <sub>4</sub>	SDLM	3.8	1.88	24.2	439
SG168-21	3045	Es <sub>4</sub>	SDLM	3.71	2.09	20.94	440
SG168-22	3051	Es <sub>4</sub>	SDLM	3.56	1.38	19.62	439
SG168-23	3057	Es <sub>4</sub>	SDLM	1.55	1.19	7.37	434
SG168-24	3063	Es <sub>4</sub>	SDLM	1.65	0.55	6.65	438
SG168-25	3069	Es <sub>4</sub>	SDLM	2.98	1.52	16.8	436
SG168-26	3075	Es <sub>4</sub>	SDLM	1.1	0.27	3.86	435
SG168-27	3081	Es <sub>4</sub>	SDLM	1.07	0.36	3.22	434
SG168-28	3087	Es <sub>4</sub>	SDLM	2.82	1.83	14.89	439
SG168-29	3093	Es <sub>4</sub>	SDLM	2.25	1.2	11.38	436
SG168-30	3099	Es <sub>4</sub>	SDLM	1.75	0.41	6.55	435
SG168-31	3105	Es <sub>4</sub>	SDLM	1.5	0.61	7.97	434
SG168-32	3111	Es <sub>4</sub>	SDLM	1.76	0.51	8.18	443
SG168-33	3117	Es <sub>4</sub>	SDLM	2.31	0.65	13.64	440
SG168-34	3123	Es <sub>4</sub>	SDLM	2.61	0.98	13.72	440
SG168-35	3129	Es <sub>4</sub>	SDLM	2.22	0.87	10.27	438
SG168-36	3135	Es <sub>4</sub>	SDLM	1.53	0.46	6.49	438
SG168-37	3141	Es <sub>4</sub>	SDLM	2.09	0.71	9.99	439
SG168-38	3147	Es <sub>4</sub>	SDLM	2.51	0.79	9.21	438
SG168-39	3153	Es <sub>4</sub>	SDLM	2.14	0.43	7.83	436
SG168-40	3159	Es <sub>4</sub>	SDLM	3.22	0.87	12.99	440
SG168-41	3165	Es <sub>4</sub>	SDLM	3.91	1.68	18.6	440
SG168-42	3171	Es <sub>4</sub>	SDLM	3.15	1.08	14.3	443
SG168-43	3177	Es <sub>4</sub>	SDLM	4.08	1.48	17.72	442
SG168-44	3183	Es <sub>4</sub>	SDLM	3.34	1.42	13.43	442
SG168-45	3189	Es <sub>4</sub>	SDLM	4.16	2.77	20.69	440
SG168-46	3195	Es <sub>4</sub>	SDLM	4.05	2.6	19.85	441
SG168-47	3201	Es <sub>4</sub>	SDLM	5.13	3.35	25.52	441
SG168-48	3207	Es <sub>4</sub>	SDLM	5.05	1.87	28.1	444
SG168-49	3213	Es <sub>4</sub>	SDLM	4.94	1.87	25.17	441
SG168-50	3219	Es <sub>4</sub>	SDLM	4.73	1.02	29.57	439
SG168-51	3225	Es <sub>4</sub>	SDLM	2.88	1.39	14.8	442
SG168-52	3231	Es <sub>4</sub>	SDLM	3.91	0.97	20.04	442
SG168-53	3237	Es <sub>4</sub>	SDLM	3.78	1.43	28.87	442
SG168-54	3243	Es <sub>4</sub>	SDLM	4.75	1.47	27.6	441
SG168-55	3249	Es <sub>4</sub>	SDLM	3.59	1.05	20.38	440

Table A1. Cont.

Sample ID	Depth (m)	Strata	Mudstone Types	TOC (%)	Pyrolysis Data		
					S <sub>1</sub> (mg/g)	S <sub>2</sub> (mg/g)	T <sub>max</sub> (°C)
MS1-1	3160	Es <sub>3</sub>	SDLM	1.68	0.103	4.77	436
MS1-2	3182	Es <sub>3</sub>	SDLM	1.82	0.35	4.77	439
MS1-3	3202	Es <sub>3</sub>	SDLM	1.85	0.26	6.49	437
MS1-4	3222	Es <sub>3</sub>	SDLM	2.61	0.54	5.87	439
MS1-5	3238	Es <sub>3</sub>	SDLM	1.78	0.42	5.59	440
MS1-6	3262	Es <sub>3</sub>	SDLM	1.66	0.35	5.56	439
MS1-7	3281	Es <sub>3</sub>	SDLM	2.15	0.44	9.87	440
MS1-8	3299	Es <sub>3</sub>	SDLM	1.81	0.38	6.05	440
MS1-9	3319	Es <sub>3</sub>	SDLM	1.93	0.31	7.16	441
MS1-10	3340	Es <sub>3</sub>	SDLM	1.94	0.46	5.65	438
MS1-11	3360	Es <sub>3</sub>	SDLM	2.13	0.46	4.51	438
MS1-12	3382	Es <sub>3</sub>	SDLM	2.17	0.98	8.03	441
MS1-13	3399	Es <sub>3</sub>	SDLM	3.01	1.06	6.65	440
MS1-14	3410	Es <sub>3</sub>	SDLM	2.26	0.34	5.45	440
MS1-15	3450	Es <sub>3</sub>	SDLM	2.47	0.33	6.92	442
MS1-16	3470	Es <sub>3</sub>	SDLM	2.21	0.51	8.09	439
MS1-17	3477	Es <sub>3</sub>	SDLM	2.01	0.29	4.24	442
MS1-18	3596	Es <sub>3</sub>	NSFM	2.09	0.41	3.33	444
MS1-19	3621	Es <sub>3</sub>	NSFM	1.71	0.49	3.46	446
MS1-20	3670	Es <sub>3</sub>	NSFM	2.34	0.63	3.03	448
MS1-21	3702	Es <sub>3</sub>	NSFM	1.64	0.43	1.89	448
MS1-22	3720	Es <sub>3</sub>	NSFM	1.91	0.34	3.59	447
MS1-23	3755	Es <sub>3</sub>	NSFM	1.81	0.56	2.23	446
MS1-24	3740	Es <sub>3</sub>	NSFM	1.72	0.48	2.74	447
MS1-25	3826	Es <sub>3</sub>	NSFM	1.63	0.51	1.47	448
MS1-26	3872	Es <sub>3</sub>	NSFM	1.93	0.56	2.11	450
MS1-27	3901	Es <sub>3</sub>	NSFM	1.57	0.72	1.86	449
MS1-28	3925	Es <sub>3</sub>	NSFM	2.16	0.65	1.99	442
MS1-29	3948	Es <sub>3</sub>	NSFM	1.66	0.92	2.61	438
MS1-30	3970	Es <sub>3</sub>	NSFM	2.45	0.81	1.42	450
MS1-31	4011	Es <sub>3</sub>	NSFM	1.73	1.06	2.02	442
MS1-32	4025	Es <sub>3</sub>	NSFM	1.78	0.84	2.02	446
MS1-33	4070	Es <sub>3</sub>	NSFM	1.61	0.78	1.88	445
MS1-34	4090	Es <sub>3</sub>	NSFM	1.68	0.84	1.56	442
MS1-35	4121	Es <sub>3</sub>	NSFM	2.27	0.58	1.17	445
MS1-36	4141	Es <sub>3</sub>	NSFM	1.64	1.97	2.68	435
MS1-37	4202	Es <sub>3</sub>	NSFM	1.94	0.66	1.56	437
MS1-38	4221	Es <sub>3</sub>	NSFM	1.57	2.36	2.48	439
MS1-39	4260	Es <sub>3</sub>	NSFM	1.72	0.71	1.27	437
MS1-40	4256	Es <sub>3</sub>	NSFM	1.67	0.69	0.94	436
MS1-41	4286	Es <sub>3</sub>	NSFM	1.97	0.98	1.58	440
MS1-42	4340	Es <sub>3</sub>	NSFM	1.73	0.92	1.33	438
MS1-43	4420	Es <sub>3</sub>	NSFM	1.72	1.52	1.31	441
MS1-44	4461	Es <sub>3</sub>	NSFM	1.68	0.65	0.95	434
MS1-45	4485	Es <sub>3</sub>	NSFM	1.67	0.64	0.96	450
MS1-46	4499	Es <sub>3</sub>	NSFM	1.53	0.84	0.95	436
MS1-47	4526	Es <sub>3</sub>	NSFM	1.69	1.41	2.22	446
MS1-48	4545	Es <sub>3</sub>	NSFM	1.81	0.68	0.87	440
MS1-49	4580	Es <sub>3</sub>	NSFM	1.73	1.35	1.62	442
MS1-50	4600	Es <sub>3</sub>	NSFM	1.75	0.39	1.35	437
MS1-51	4620	Es <sub>3</sub>	NSFM	1.82	0.31	0.74	437
MS1-52	4641	Es <sub>3</sub>	NSFM	1.77	0.83	1.27	443
MS1-53	4652	Es <sub>3</sub>	NSFM	2.18	0.66	0.65	448



Table A1. Cont.

Sample ID	Depth (m)	Strata	Mudstone Types	TOC (%)	Pyrolysis Data		
					S <sub>1</sub> (mg/g)	S <sub>2</sub> (mg/g)	T <sub>max</sub> (°C)
MT1-1	4226	Es <sub>3</sub>	NSFM	1.45	0.735	2.175	395
MT1-2	4302	Es <sub>3</sub>	NSFM	1.9	0.833	2.527	400
MT1-3	4320	Es <sub>3</sub>	NSFM	1.36	0.6164	2.0536	399
MT1-4	4344	Es <sub>3</sub>	NSFM	1.78	0.5958	2.4742	400
MT1-5	4378	Es <sub>3</sub>	NSFM	2.1	0.85	2.73	399
MT1-6	4392	Es <sub>3</sub>	NSFM	1.97	0.9984	2.5216	398
MT1-7	4422	Es <sub>3</sub>	NSFM	1.93	0.6989	2.4511	399
MT1-8	4500	Es <sub>3</sub>	NSFM	1.72	0.654	1.806	392
MT1-9	4518	Es <sub>3</sub>	NSFM	1.4	0.338	1.302	392
MT1-10	4544	Es <sub>3</sub>	NSFM	2.11	0.7037	2.8063	432
MT1-11	4694	Es <sub>3</sub>	NSFM	1.85	0.384	1.776	395
MT1-12	4720	Es <sub>3</sub>	NSFM	1.77	0.2708	1.6992	393
MT1-13	4736	Es <sub>3</sub>	NSFM	1.76	0.3456	1.6544	388
MT1-14	4798	Es <sub>3</sub>	NSFM	1.97	0.4879	1.8321	395
MT1-15	4844	Es <sub>3</sub>	NSFM	2.07	0.5542	1.9458	392
MT1-16	5104.4	Es <sub>3</sub>	NSFM	1.29	0.0091	0.2709	554
MT1-17	5105.5	Es <sub>3</sub>	NSFM	1.11	0.0147	0.2553	568
MT1-18	5107	Es <sub>3</sub>	NSFM	1.2	0.016	0.324	550
MT1-19	5734	Es <sub>3</sub>	NSFM	1.31	0.24	0.47	379
MT1-20	5782	Es <sub>3</sub>	NSFM	1.046	0.26	0.51	376

Table A2. Molecular and carbon isotopic composition of all natural gas samples.

Sample ID	Strata	CompimENTS (%)							$\delta^{13}\text{C}$ (‰, VPDB)					
		N <sub>2</sub>	CO <sub>2</sub>	CH <sub>4</sub>	C <sub>2</sub> H <sub>6</sub>	C <sub>3</sub> H <sub>8</sub>	iC <sub>4</sub> H <sub>10</sub>	nC <sub>4</sub> H <sub>10</sub>	$\delta^{13}\text{C}_{\text{CO}_2}$	$\delta^{13}\text{C}_1$	$\delta^{13}\text{C}_2$	$\delta^{13}\text{C}_3$	$\delta i\text{C}_4$	$\delta n\text{C}_4$
X1	Ed	/	/	97.64	1.04	0	0.25	0.1	/	−44.0	/	/	/	/
X2	Ed	0.12	0.16	98.64	0.74	0.02	0.31	0	/	−42.4	−22.1	−7.0	/	/
X3	Ed	0.09	0.34	98.42	0.75	0.04	0.29	0.01	−12.3	−43.3	−22.5	−14.5	−26.9	−19.4
X4	Ed	0.15	0	98.3	1.37	0.02	0.13	0	/	−44.4	−25.8	−9.6	−26.9	/
X5	Ed	0.1	0	98.18	1.3	0.07	0.25	0.02	/	−43.2	−25.1	−13.5	−28.0	/
X6	Ed	0.06	0.18	98.39	0.97	0.05	0.19	0.01	−18.3	−43.8	−25.5	−18.7	−25.2	−21.0
X7	Ed	0.01	0	97.01	2.17	0.13	0.44	0.02	−20.4	−44.2	−26.2	−15.0	−28.0	−19.8
X8	Ed	0.11	0	97.56	1.7	0.09	0.34	0.02	/	−43.7	−26.1	−14.6	−28.0	/
X9	Ed	0.11	0	97.37	1.85	0.12	0.35	0.03	−20.6	−43.8	−26.1	−14.8	−27.9	−19.6
X10	Ed	0.1	0.32	96.48	1.94	0.34	0.36	0.08	−18.7	−42.7	−25.6	−19.9	−27.4	−20.8
X11	Ed	/	/	98.24	0.71	0	0.09	0	/	−44.9	/	/	/	/
X12	Ed	0.1	0	97.54	1.84	0.09	0.34	0.01	−21.1	−43.6	−26.0	−12.8	−28.1	/
X13	Ed	0.09	0.15	97.01	2.03	0.12	0.35	0.03	/	−43.7	−26.1	−15.0	−28.2	−20.4
X14	Ed	0.15	0	97.78	1.72	0.03	0.3	0	/	−44.2	−26.1	−8.8	−27.8	/
X15	Ed	0.17	0	97.05	2.16	0.3	0.19	0.05	/	−44.4	−26.6	−22.0	−27.1	−20.6
X16	Ed	0.05	0.33	96.53	2.29	0.13	0.39	0.02	/	−42.8	−26.1	−13.2	−28.9	−17.4
X17	Ed	0.11	0	97.64	1.85	0.06	0.32	0	−21.3	−44.1	−25.9	−10.0	−28.2	/
X18	Ed	0.26	0	99.52	0.18	0.02	0.02	0.01	−18.4	−51.3	−25.5	/	/	/
X19	Ed	0.22	0	97.89	1.56	0.14	0.09	0.04	/	−52.1	−31.8	/	/	/
X20	Ed	0.31	0	99.46	0.22	0	0.01	0	−20.8	−50.6	−27.7	/	/	/
X21	Ed	0.23	0	97.72	1.75	0.08	0.1	0.03	/	−52.4	−31.4	−19.8	−27.3	−21.3
X22	Ed	0.24	0	97.56	1.73	0.13	0.22	0.03	/	−51.0	−29.1	−18.2	−28.0	−22.5
X23	Ed	0.37	0	99.5	0.13	0	0	0	−20.3	−51.9	−34.8	/	/	/
X24	Ed	0.21	0	97.4	1.74	0.28	0.16	0.09	/	−51.0	−30.7	−21.3	−28.0	−24.0
X25	Ed	0.25	0.76	84.75	7.89	4.34	0.52	0.95	−3.1	−45.7	−30.4	−27.8	/	−26.7
X26	Es <sub>1</sub>	0.13	1.5	82.46	8.81	4.59	0.58	1.09	−4.2	−45.4	−31.1	−28.0	/	−26.8
X27	Es <sub>1</sub>	2.44	19.65	77.44	0.31	0.05	0.01	0.00	−0.7	−28.6	−18.9	−18.6	/	/
X28	Es <sub>3</sub>	1.19	20.37	78.24	0.11	0.01	0.00	0.00	−2.4	−28.7	−17.5	/	/	/
X29	Es <sub>3</sub>	2	0.16	91.77	4.8	0.7	0.12	0.26	−6.0	−31.0	−24.8	−23.8	−23.9	/
X30	Ar	2.12	0.28	85.21	5.08	2.8	1.01	1.29	−6.8	−31.9	−26.2	−25.7	−25.7	/
X31	Ar	1.7	0.1	90.1	4.4	1.9	0.6	0.8	−	−36.37	−25.30	−24.30	/	/
X32	Ar	0.83	0.45	85.7	7.14	3.16	0.84	1.04	−2.7	−37.2	−27.0	−25.9	−25.6	/
X33	Ar	30.16	0.073	63.39	4.63	0.7	0.12	0.28	−	−36.3	−26.6	−24.5	−24.0	/
X34	Ar	31.17	0.15	62.65	4.76	0.56	0.061	0.14	−	−37.2	−27.2	−24.7	−23.1	/
X35	Ar	0.8	0.46	83.49	9	3.57	0.77	0.85	−11.8	−36.6	−27.4	−25.6	−25.7	/
X36	Ar	1.31	0.19	85.51	7.37	3.31	0.77	0.9	−	−36.8	−27.6	−25.8	−24.8	/
X37	Ar	/	/	97.64	1.04	0	0.25	0.1	/	−44.0	/	/	/	/

## References

- Gawthorpe, R.; Leeder, M. Tectono-sedimentary evolution of active extensional basins. *Basin Res.* **2000**, *12*, 195–218. [\[CrossRef\]](#)
- Liu, G.; Zeng, L.; Li, H.; Ostadhassan, M.; Rabiei, M. Natural fractures in metamorphic basement reservoirs in the Liaohe Basin, China. *Mar. Pet. Geol.* **2020**, *119*, 104479. [\[CrossRef\]](#)
- Hou, M.; Cao, H.; Li, H.; Chen, A.; Wei, A.; Chen, Y.; Wang, Y.; Zhou, X.; Ye, T. Characteristics and controlling factors of deep buried-hill reservoirs in the BZ19-6 structural belt, Bohai Sea area. *Nat. Gas Ind. B* **2019**, *6*, 305–316. [\[CrossRef\]](#)
- Meng, W.; Chen, Z.; Li, P.; Guo, Y.; Gao, X.; Hui, X.; Zhang, Y. Exploration theories and practices of buried-hill reservoirs: A case from Liaohe Depressions. *Pet. Explor. Dev.* **2009**, *36*, 136–143. (In Chinese)
- Feng, Y.; Liu, G.; Yang, W.; Gong, Y. Characteristics and model of reservoir formation in Xinglongtai oilfield, Liaohe depression. *Mar. Geol. Quat. Geol.* **2014**, *34*, 137–143. (In Chinese)
- Gao, X.; Pang, X.; Li, X.; Chen, Z.; Shan, J.; Liu, F.; Zou, Z.; Li, W. Characteristics of oil and gas complex formation and the series of oil and gas reservoirs in the submerged mountain tectonic zone of the faulted basin—Taking the Xinglongtai tectonic zone of the western Liaohe depression as an example. *Sci. Sin.* **2008**, *38*, 95–102. (In Chinese)
- Pei, L.; Wang, X.; Gao, G.; Liu, W. Geochemical heterogeneity, origin and secondary alteration of natural gas inside and outside buried hills of Xinglongtai area, West Sag, Liaohe Depression, Bohai Bay Basin. *J. Pet. Sci. Eng.* **2022**, *208*, 109456. [\[CrossRef\]](#)
- Pei, L.; Wang, X.; Wang, Q.; Zhang, Q.; Luo, H.; Liu, W. Origin, accumulation and secondary alteration of natural gas around Qingshui Sub-sag, Liaohe Depression, China: Insights from molecular and isotopic composition. *Mar. Pet. Geol.* **2022**, *135*, 105390. [\[CrossRef\]](#)
- Li, X. Accumulation conditions and key exploration & development technologies of heavy oil in Huanxiling oilfield in Liaohe depression, Bohai Bay Basin. *Pet. Res.* **2020**, *5*, 18–38.
- Liu, Q.; Wu, X.; Wang, X.; Jin, Z.; Zhu, D.; Meng, Q.; Huang, S.; Liu, J.; Fu, Q. Carbon and hydrogen isotopes of methane, ethane, and propane: A review of genetic identification of natural gas. *Earth Sci. Rev.* **2019**, *190*, 247–272. [\[CrossRef\]](#)
- Xu, C.; Yu, H.; Wang, J.; Liu, X. Formation conditions and accumulation characteristics of Bozhong 19-6 large condensate gas field in offshore Bohai Bay Basin. *Pet. Explor. Dev.* **2019**, *46*, 27–40. [\[CrossRef\]](#)
- Wang, Q.; Hao, F.; Niu, C.; Zou, H.; Miao, Q.; Yin, J.; Cao, Y.; Liu, M. Origins and deep petroleum dynamic accumulation in the southwest part of the Bozhong depression, Bohai Bay Basin: Insights from geochemical and geological evidences. *Mar. Pet. Geol.* **2021**, *134*, 105347. [\[CrossRef\]](#)
- Wang, J.-Y.; Wang, J.-A.; Xiong, L.-P.; Zhang, J.-M. Analysis of factors affecting heat flow density determination in the Liaohe Basin, North China. *Tectonophysics* **1985**, *121*, 63–78. [\[CrossRef\]](#)
- Qi, J.; Yang, Q. Cenozoic structural deformation and dynamic processes of the Bohai Bay basin province, China. *Mar. Pet. Geol.* **2010**, *27*, 757–771. [\[CrossRef\]](#)
- Li, M.; Qi, J.; Tong, H.; Yu, F.; Wang, N. Cenozoic fault structure and hydrocarbon accumulation in Western Sag, Liaohe Depression. *Pet. Explor. Dev.* **2010**, *37*, 281–288. (In Chinese)
- Hu, L.; Fuhrmann, A.; Poelchau, H.S.; Horsfield, B.; Zhang, Z.; Wu, T.; Chen, Y.; Li, J. Numerical simulation of petroleum generation and migration in the Qingshui sag, western depression of the Liaohe basin, northeast China. *AAPG Bull.* **2005**, *89*, 1629–1649. [\[CrossRef\]](#)
- Wang, Y.; Hu, Y.; Huang, S.; Kang, W.; Chen, Y. Geological conditions, potential and exploration direction of nature gas in Liaohe Depression, Bohai Bay Basin. *Natural Gas Geosci.* **2018**, *29*, 1422–1432. (In Chinese)
- Peng, W.; Hu, G.; Feng, Z.; Liu, D.; Wang, Y.; Lv, Y.; Zhao, R. Origin of Paleogene natural gases and discussion of abnormal carbon isotopic composition of heavy alkanes in the Liaohe Basin, NE China. *Mar. Pet. Geol.* **2018**, *92*, 670–684. [\[CrossRef\]](#)
- Mu, G.; Zhong, N.; Liu, B.; Yu, T.; Liu, Y. The quantitative evaluation method of lacustrine mudstone source rock and its application. *Acta Pet. Sin.* **2010**, *31*, 218–224+230. (In Chinese)
- Wang, Y.; Chen, J.; Shen, W.; Gao, X.; Li, S. Anomalies of gas molecular and isotopic compositions of terrestrial mud volcanoes caused by post-genetic processes—A case from the mud volcanoes in the Junggar Basin, northwest China. *J. Pet. Sci. Eng.* **2021**, *196*, 107698. [\[CrossRef\]](#)
- Wang, X.; Jiang, Z.; Hu, G.; Fan, T.; Wang, J.; Lu, H. Sedimentary facies and evolution of upper fourth member of paleogene shahejie formation in western sag of Liaohe Basin. *J. Jilin Univ. Earth Sci. Ed.* **2019**, *49*, 1222–1234. (In Chinese)
- Shabani, F.; Amini, A.; Tavakoli, V.; Chehrizi, A.; Gong, C. 3D basin and petroleum system modelling of the early cretaceous play in the NW Persian Gulf. *Geoenvironment Sci. Eng.* **2023**, *226*, 211768. [\[CrossRef\]](#)
- Baur, F.; Hosford Scheirer, A.; Peters, K.E. Past, present, and future of basin and petroleum system modeling. *AAPG Bull.* **2018**, *102*, 549–561. [\[CrossRef\]](#)
- Abdel-Fattah, M.I.; Pigott, J.D.; Abd-Allah, Z.M. Integrative 1D-2D basin modeling of the cretaceous Beni Suef basin, Western Desert, Egypt. *J. Pet. Sci. Eng.* **2017**, *153*, 297–313. [\[CrossRef\]](#)
- Al-Hajeri, M.M.; Al Saeed, M.; Derks, J.; Fuchs, T.; Hantschel, T.; Kauerauf, A.; Neumaier, M.; Schenk, O.; Swientek, O.; Tessen, N. Basin and petroleum system modeling. *Oilfield Rev.* **2009**, *21*, 14–29.
- Yang, S.; Li, M.; Xiao, H.; Wang, F.; Cai, G.; Huang, S. Prediction and quantification of effective gas source rocks in a lacustrine basin: Western Depression in the Liaohe Subbasin. *Pet. Sci.* **2023**. under review.
- Burnham, A.K. *A Simple Kinetic Model of Petroleum Formation and Cracking*; Lawrence Livermore National Lab.: Livermore, CA, USA, 1989.

28. Chen, L.; Gan, H.; Zhu, C.; Tian, J. Study on Subsidence History of Weixinan Sag, Beibuwan Basin. *J. Xinjiang Pet. Inst.* **2002**, *14*, 12–17. (In Chinese)
29. Wygrala, B.P. *Integrated Study of an Oil Field in the Southern Po Basin, Northern Italy*; KFK: Karlsruhe, Germany, 1989; 325p.
30. Peters, K.E. Guidelines for evaluating petroleum source rock using programmed pyrolysis. *AAPG Bull.* **1986**, *70*, 318–329.
31. Liu, Q.; Jin, Z.; Meng, Q.; Wu, X.; Jia, H. Genetic types of natural gas and filling patterns in Daniudi gas field, Ordos Basin, China. *J. Asian Earth Sci.* **2015**, *107*, 1–11. [[CrossRef](#)]
32. Dai, J.; Ni, Y.; Huang, S.; Peng, W.; Han, W.; Gong, D.; Wei, W. Genetic types of gas hydrates in China. *Pet. Explor. Dev.* **2017**, *44*, 887–898. [[CrossRef](#)]
33. Chung, H.M.; Gormly, J.R.; Squires, R.M. Origin of gaseous hydrocarbons in subsurface environments: Theoretical considerations of carbon isotope distribution. *Chem. Geol.* **1988**, *71*, 97–104. [[CrossRef](#)]
34. Whiticar, M.J. Carbon and hydrogen isotope systematics of bacterial formation and oxidation of methane. *Chem. Geol.* **1999**, *161*, 291–314. [[CrossRef](#)]
35. Milkov, A.V.; Etiope, G. Revised genetic diagrams for natural gases based on a global dataset of >20,000 samples. *Org. Geochem.* **2018**, *125*, 109–120. [[CrossRef](#)]
36. Liu, W.; Zhang, D.; Gao, B.; Fan, M. Using geochemical tracing system to identify new types of gas sources in marine strata of the Hotan River Gas Field in the Tarim Basin. *Sci. China Earth Sci.* **2010**, *53*, 844–853. [[CrossRef](#)]
37. Dai, J.; Li, J.; Luo, X.; Zhang, W.; Hu, G.; Ma, C.; Guo, J.; Ge, S. Stable carbon isotope compositions and source rock geochemistry of the giant gas accumulations in the Ordos Basin, China. *Org. Geochem.* **2005**, *36*, 1617–1635. [[CrossRef](#)]
38. Dai, J. Identification of various alkane gases. *Sci. Sin.* **1992**, *2*, 185–193. (In Chinese)
39. Song, Y.; Zhao, M.; Hu, G.; Zhu, G. Progress and prospects of natural gas geochemical research in China. *Bull. Mineral. Petrol. Geochem.* **2012**, *31*, 529–542. (In Chinese)
40. James, A.; Burns, B. Microbial alteration of subsurface natural gas accumulations. *AAPG Bull.* **1984**, *68*, 957–960.
41. Li, M.; Lai, H.; Mao, F.; Liu, G.; Xiao, H.; Tang, Y. Geochemical assessment of source rock within a stratigraphic geochemical framework: Taking Termit Basin (Niger) as an example. *Earth Sci.* **2018**, *43*, 3603–3615. (In Chinese)
42. Lai, H.; Li, M.; Liu, J.; Mao, F.; Xiao, H.; He, W.; Yang, L. Organic geochemical characteristics and depositional models of Upper Cretaceous marine source rocks in the Termit Basin, Niger. *Palaeogeogr. Palaeoclimatol. Palaeoecol.* **2018**, *495*, 292–308. [[CrossRef](#)]
43. Li, M.; Zhong, N.; Shi, S.; Zhu, L.; Tang, Y. The origin of trimethyldibenzothiophenes and their application as maturity indicators in sediments from the Liaohe Basin, East China. *Fuel* **2013**, *103*, 299–307. [[CrossRef](#)]
44. Xie, Y.; Zhu, X.; Zhao, K. Sequence-stratigraphic Framework on Paleogene of the Liaohe Western Depression. *Sci. Technol. Rev.* **2010**, *28*, 58–64. (In Chinese)
45. Yang, T.; Cao, Y.; Liu, H. Highstand sublacustrine fans: The role of a sudden increase in sediment supply. *Basin Res.* **2023**, *35*, 1486–1508. [[CrossRef](#)]
46. Yang, T.; Cao, Y.; Wang, Y.; Cai, L.; Liu, H.; Jin, J. Sedimentary characteristics and depositional model of hyperpycnites in the gentle slope of a lacustrine rift basin: A case study from the third member of the Eocene Shahejie Formation, Bonan Sag, Bohai Bay Basin, Eastern China. *Basin Res.* **2023**, *35*, 1590–1618. [[CrossRef](#)]
47. Welte, D.; Tissot, P. *Petroleum Formation and Occurrence*; Springer: Berlin/Heidelberg, Germany, 1984.
48. Makeen, Y.M.; Abdullah, W.H.; Pearson, M.J.; Hakimi, M.H.; Ayinla, H.A.; Elhassan, O.M.; Abas, A.M. History of hydrocarbon generation, migration and accumulation in the Fula sub-basin, Muglad Basin, Sudan: Implications of a 2D basin modeling study. *Mar. Pet. Geol.* **2016**, *77*, 931–941. [[CrossRef](#)]

**Disclaimer/Publisher’s Note:** The statements, opinions and data contained in all publications are solely those of the individual author(s) and contributor(s) and not of MDPI and/or the editor(s). MDPI and/or the editor(s) disclaim responsibility for any injury to people or property resulting from any ideas, methods, instructions or products referred to in the content.